The Astrophysical Journal, 806:160 (18pp), 2015 June 20 doi:10.1088/0004-637X/806/2/160

SN 2013ej: A TYPE IIL SUPERNOVA WITH WEAK SIGNS OF INTERACTION

Subhash Bose[1,2], Firoza Sutaria[3], Brijesh Kumar[1], Chetna Duggal[3], Kuntal Misra[1], Peter J. Brown[4], Mridweeka Singh[1], Vikram Dwarkadas[5], Donald G. York[6], Sayan Chakraborti[7], H. C. Chandola[2], Julie Dahlstrom[8], Alak Ray[9], and Margarita Safonova[3]

[1] Aryabhatta Research Institute of Observational Sciences, Manora Peak, Nainital 263002, India; email@subhashbose.com, bose@aries.res.in
[2] Centre of Advance Study, Department of Physics, Kumaun University, Nainital 263001, India
[3] Indian Institute of Astrophysics, Block-II, Koramangala, Bangalore 560034, India
[4] George P. and Cynthia Woods Mitchell Institute for Fundamental Physics & Astronomy, Texas A&M University, Department of Physics and Astronomy, 4242 TAMU, College Station, TX 77843, USA
[5] Department of Astronomy and Astrophysics, University of Chicago, Chicago, IL 60637, USA
[6] Department of Astronomy and Astrophysics and The Enrico Fermi Institute, University of Chicago, Chicago, IL 60637, USA
[7] Institute for Theory and Computation, Harvard-Smithsonian Center for Astrophysics, 60 Garden Street, Cambridge, MA 02138, USA
[8] Carthage College, 2001 Alford Park Dr., Kenosha, WI 53140, USA
[9] Tata Institute of Fundamental Research, Homi Bhabha Road, Mumbai 400005, India
Received 2015 March 3; accepted 2015 April 23; published 2015 June 15

ABSTRACT

We present optical photometric and spectroscopic observations of SN 2013ej. It is one of the brightest Type II supernovae (SNe II) exploded in a nearby (∼10 Mpc) galaxy, NGC 628. The light-curve characteristics are similar to SNe II, but with a relatively shorter (∼85 days) and steeper (∼1.7 mag (100 days)$^{-1}$ in V) plateau phase. The SN shows a large drop of 2.4 mag in V-band brightness during the plateau-to-nebular transition. The absolute ultraviolet (UV) light curves are identical to SN 2012aw, showing a similar UV-plateau trend extending up to 85 days. The radioactive ^{56}Ni mass estimated from the tail luminosity is 0.02 $M_{\odot}$, which is significantly lower than typical SNe IIP. The characteristics of spectral features and evolution of line velocities indicate that SN 2013ej is a Type II event. However, light-curve characteristics and some spectroscopic features provide strong support in classifying it as a Type IIL event. A detailed SYNOW modeling of spectra indicates the presence of some high-velocity components in Hα and Hβ profiles, implying a possible ejecta–circumstellar medium interaction. The nebular phase spectrum shows an unusual notch in the Hα emission, which may indicate bipolar distribution of ^{56}Ni. Modeling of the bolometric light curve yields a progenitor mass of ∼14 $M_{\odot}$ and a radius of ∼450 $R_{\odot}$, with a total explosion energy of $\sim 2.3 \times 10^{51}$ erg.

Key words: galaxies: individual (NGC 0628) – supernovae: general – supernovae: individual (SN 2013ej)

1. INTRODUCTION

Type II supernovae (SNe II) originate from massive stars with $M_{\rm ZAMS} > 8\ M_{\odot}$ (Burrows 2013) that have retained substantial hydrogen in the envelope at the time of explosion. They belong to a subclass of core-collapse SNe (CCSNe), which collapse under their own gravity at the end of the nuclear burning phase, having insufficient thermal energy to withstand the collapse.

The most common subtype among hydrogen-rich supernovae is Type IIP. At the time of shock breakout almost the entire mass of hydrogen is ionized. SNe IIP have an extended hydrogen envelope, which recombines slowly over a prolonged duration, sustaining the plateau phase. During this phase, the SN light curve shows almost constant brightness lasting for 80–100 days. At the end of the plateau phase, the SN experiences a sudden drop in luminosity, settling onto the slow declining radioactive tail, also known as the nebular phase, which is mainly powered by gamma rays released from the decay of ^{56}Co to ^{56}Fe, which in turn depends on the amount of ^{56}Ni synthesized at the time of explosion.

The plateau slope of the SN II light curve primarily depends on the amount of hydrogen present in the ejecta. If hydrogen content is high, as in Type IIP, the initial energy deposited from shock and decay of freshly produced ^{56}Ni shall be released slowly over a longer period of time. On the other hand, if hydrogen content is relatively low, the light curve will decline fast but with higher peak luminosity. Thus, if hydrogen content is low enough, one would expect a linear decline in the light curve, classifying it as Type IIL. By the historical classification, Type IIL (Barbon et al. 1979) shows linear decline in light curve over 100 days until it reaches the radioactive tail phase. Arcavi et al. (2012) claimed to find Type IIP and IIL as two distinct groups of events, which may further indicate their distinct class of progenitors. However, recent studies by Anderson et al. (2014b) and Sanders et al. (2015) on large samples of SNe II do not favor any such bi-modality in the diversity; rather, they found continuum in light-curve slopes and in other physical parameters. The continuous distribution of plateau slopes in Type II events is rather governed by variable amount of hydrogen mass left in the envelope at the time of explosion. Based on a sample of 11 Type IIL events, Faran et al. (2014) proposed that any event having a decline of 0.5 mag in the V-band light curve in the first 50 days can be classified as Type IIL. In light of these recent developments, a large number of SNe IIP classified earlier may now fall under the IIL class. Thus, many of the past studies collectively on samples of SNe IIP, to which we shall be referring in this work, may include both IIP and IIL.

Extensive studies have been done to relate observable parameters and progenitor properties of SNe IIP (e.g., Litvinova & Nadezhin 1985; Hamuy 2003). Stellar evolutionary models suggest that these SNe may originate from stars with zero-age main-sequence mass of 9–25 $M_{\odot}$ (e.g., Heger et al. 2003). However, progenitors directly recovered for a

Table 1
Relevant Parameters for the Host Galaxy NGC 0628 and SN 2013ej

Parameters	Value	References
NGC 0628:		
Alternate name	M74	2
Type	Sc	2
R.A. (J2000)	$\alpha = 01^{h}36^{m}41\overset{s}{.}77$	2
Decl. (J2000)	$\delta = 15°46' 59\overset{''}{.}8$	2
Abs. magnitude	$M_B = -20.72$ mag	2
Distance	$D = 9.6 \pm 0.7$ Mpc	1
Distance modulus	$\mu = 29.90 \pm 0.16$ mag	...
Heliocentric velocity	$cz_{\rm helio} = 658 \pm 1$ km s^{-1}	2
SN 2013ej:		
R.A. (J2000)	$\alpha = 01^{h}36^{m}48\overset{s}{.}16$	3
Decl. (J2000)	$\delta = 15°45' 31\overset{''}{.}3$	...
Galactocentric location	$1'33''$ E, $2'15''$ S	...
Date of explosion	$t_0 = 23.8$ 2013 Jul (UT)	1
	(JD 2456497.3 ± 0.3)	...
Reddening	$E(B-V) = 0.060 \pm 0.001$ mag	1

References. (1) This paper; (2) HyperLEDA, http://leda.univ-lyon1.fr; (3) Kim et al. (2013).

number of nearby SNe IIP, using the pre-SN *Hubble Space Telescope* (*HST*) archival images, are found to lie within 8–17 $M_\odot$ RSG stars (Smartt 2009). A recent X-ray study also infers an upper mass limit of $<19\,M_\odot$ for Type IIP progenitors (Dwarkadas 2014), which is in close agreement with that obtained from direct detection of progenitors.

The geometry of the explosion and presence of preexistent circumstellar medium (CSM), often associated with progenitor mass loss during the late stellar evolutionary phase, can significantly alter the observables even though originating from similar progenitors. There are number of recent studies of SNe II, like 2007od (Inserra et al. 2011), 2009bw (Inserra et al. 2012), and 2013by (Valenti et al. 2015), that show a signature of such CSM interactions during various phases of evolution.

SN 2013ej is one of the youngest detected SNe II that was discovered soon after its explosion. The earliest detection was reported on 2013 July 24.125 UTC by C. Feliciano in *Bright Supernovae*,[10] along with a subsequent independent detection on July 24.83 UTC by Lee et al. (2013) at *V*-band magnitude of ~14.0. The last non-detection was reported on 2013 July 23.54 UTC by the All Sky Automated Survey for Supernovae (Shappee et al. 2013) at a *V*-band detection limit of >16.7 mag. Therefore, we adopt an explosion epoch (0d) of July 23.8 UTC (JD = 2,456,497.3 ± 0.3), which is chosen in between the last non-detection and first detection of SN 2013ej. This being one of the nearest and brightest events, it provides us with an excellent opportunity to study the origin and evolution of SNe II. Some of the basic properties of SN 2013ej and its host galaxy are listed in Table 1.

Valenti et al. (2014) presented early observations of SN 2013ej, and using temperature evolution for the first week, they estimated a progenitor radius of 400–600 $R_\odot$. Fraser et al. (2014) used high-resolution archival images from *HST* to examine the location of SN 2013ej and identified the progenitor candidate to be a supergiant of mass 8–15.5 $M_\odot$. Leonard et al. (2013) reported unusually high polarization using spectropolarimetric observation for the week-old SN, implying substantial asymmetry in the scattering atmosphere of ejecta. X-ray emission has also been detected by *Swift* XRT (Margutti et al. 2013), which may indicate that SN 2013ej has experienced CSM interaction.

In this work we present photometric and spectroscopic observation of SN 2013ej and carry out qualitative as well as quantitative analysis of the various observables through modeling and comparison with other archetypal SNe. The paper is organized as follows. In Section 2 we describe photometric and spectroscopic observations and data reduction. The estimation of line-of-sight extinction is discussed in Section 3. In Section 4 we analyze the light curves and compare absolute magnitude light curves and color curves. We also derive bolometric luminosities and estimate nickel mass from the tail luminosity. Optical spectra are analyzed in Section 5, where we model and discuss evolution of various spectral features and compare velocity profiles with other SNe II. In Section 7, we model the bolometric light curve of SN 2013ej and estimate progenitor and explosion parameters. Finally, in Section 8, we summarize the results of this work.

2. OBSERVATION AND DATA REDUCTION

2.1. Photometry

Broadband photometric observations in *UBVRI* filters have been carried out from 2.0 m IIA Himalayan Chandra Telescope (HCT) at Hanle and ARIES 1.0 m Sampurnanand Telescope (ST) and 1.3 m Devasthal Fast Optical Telescope (DFOT) at Nainital. Additionally, SN 2013ej has been also observed with *Swift* Ultraviolet/Optical Telescope (UVOT) in all six bands.

Photometric data reductions follow the same procedure as described in Bose et al. (2013). Images are cleaned and processed using standard procedures of IRAF software. DAOPHOT routines have been used to perform point-spread function photometry and extract differential light curves. To standardize the SN field, three Landolt standard fields (PG 0231, PG 2231, and SA 92) were observed on 2013 October 27 with 1.0 m ST under good photometric night and seeing (typical FWHM $\sim 2\overset{''}{.}1$ in *V* band) condition. For atmospheric extinction measurement, PG 2231 and PG 0231 were observed at different air masses. The SN field has been also observed in between standard observations. The standardization coefficients derived are represented in the following transformation equations:

$$u = U + (7.800 \pm 0.005) - (0.067 \pm 0.009) \cdot (U - B)$$
$$b = B + (5.269 \pm 0.007) - (0.060 \pm 0.009) \cdot (B - V)$$
$$v = V + (4.677 \pm 0.004) - (0.056 \pm 0.005) \cdot (B - V)$$
$$r = R + (4.405 \pm 0.005) - (0.038 \pm 0.010) \cdot (V - R)$$
$$i = I + (4.821 \pm 0.006) - (0.048 \pm 0.006) \cdot (V - I)$$

where *u*, *b*, *v*, *r*, and *i* are instrumental magnitudes corrected for time, aperture, and airmass, and *U*, *B*, *V*, *R*, and *I* are standard magnitudes. The standard deviations of the difference between the calibrated and the standard magnitudes of the observed Landolt stars are found to be ~0.03 mag in *U*, ~0.02 mag in *BR*, and ~0.01 mag in *VI*. The transformation coefficients were then used to generate eight local standard stars in the field of SN 2013ej, which are verified to be non-variable and have brightness similar to the SN. These stars are identified in Figure 1, and the calibrated *UBVRI* magnitudes are listed in

[10] http://www.rochesterastronomy.org/supernova.html

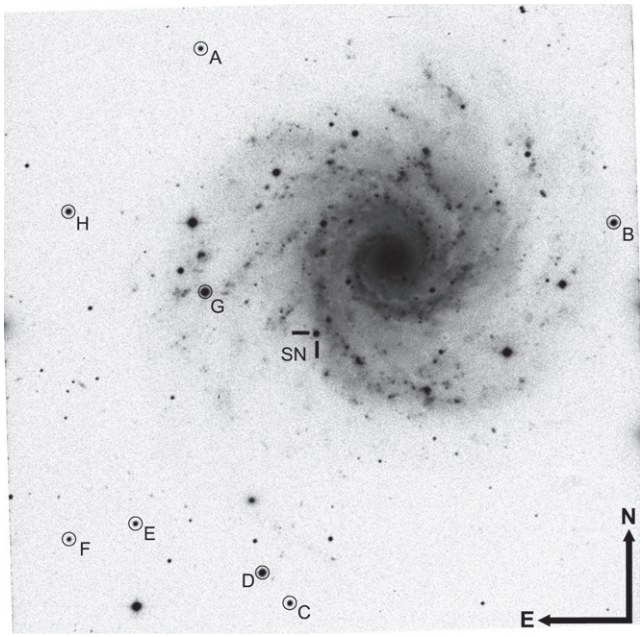

Figure 1. SN 2013ej in NGC 0628. The *BR*-band composite image taken from 104 cm ST, covering an area of about $13' \times 13'$ is shown. Eight local field standards and the SN are marked in the image.

Table 2. These selected eight local standards were further used to standardize the instrumental light curve of the SN. One of these stars (star B) is common to that used in the study by Richmond (2014), and its *BVRI* magnitudes are found to lie within 0.03 mag of our calibrated magnitudes. Our calibrated magnitudes for SN 2013ej are also found to be consistent within errors with that presented in earlier studies of the event (Valenti et al. 2014; Richmond 2014). The standard photometric magnitudes of SN 2013ej are listed in Table 3.

This SN was also observed with UVOT (Roming et al. 2005) in six bands (viz., *uvw2*, *uvm2*, *uvw1*, *uvu*, *uvb*, *uvv*) on the *Swift* spacecraft (Gehrels et al. 2004). The UV photometry was obtained from the *Swift* Optical/Ultraviolet Supernova Archive[11] (SOUSA; Brown et al. 2014). The reduction is based on that of Brown et al. (2009), including subtraction of the host galaxy count rates, and uses the revised UV zero points and time-dependent sensitivity from Breeveld et al. (2011). The UVOT photometry is listed in Table 3. The first month of UVOT photometry was previously presented by Valenti et al. (2014).

2.2. Spectroscopy

Spectroscopic observations have been carried out at 10 phases during 12–125 days. Out of these, nine epochs of low-resolution spectra are obtained from Himalaya Faint Object Spectrograph and Camera (HFOSC) mounted on the 2.0 m HCT. Spectroscopy on the HCT/HFOSC was done using a slit width of 1.92 arcsec, and grisms with resolution $\lambda/\Delta\lambda = 1330$ for Gr7 and 2190 for Gr8, and bandwidth coverage of 0.38–0.64 μm and 0.58–0.84 μm, respectively. One high-resolution spectrum is obtained from the ARC Echelle Spectrograph (ARCES) mounted on the 3.5 m ARC telescope located at Apache Point Observatory (APO). ARCES is a high-resolution cross-dispersion echelle spectrograph; the spectrum is recorded in 107 echelle orders covering a wavelength range of $\lambda \sim 0.32$–1.00 μm, at a resolution of $R \sim 31{,}500$ (Wang et al. 2003). A summary of spectroscopic observations is given in Table 4.

Spectroscopic data reduction was done under the IRAF environment. Standard reduction procedures are followed for bias subtraction and flat fielding. Cosmic-ray rejections are done using a Laplacian kernel detection algorithm for spectra, L.A.Cosmic (van Dokkum 2001). One-dimensional low-resolution spectra were extracted using the APALL task. Wavelength calibration was done using the IDENTIFY task applied on FeNe and FeAr (for HCT) arc spectra taken during observation. Wavelength calibration was cross-checked against the [O I] λ5577 sky line in the sky spectrum, and it was found to lie within 0.3–4.5 Å of the actual value. Spectra were flux-calibrated using STANDARD, SENSFUNC, and CALIBRATE tasks in IRAF. For flux calibration, spectrophotometric standards were used that were observed on the same nights as the SN spectra were recorded. All spectra were tied to the absolute flux scale using the observed flux from *UBVRI* photometry of the SN. To perform the tying, the individual spectrum is multiplied by a wavelength-dependent polynomial, which is convolved with *UBVRI* filters and then the polynomial is tuned to match the convolved flux with observations. The one-dimensional calibrated spectra were corrected for heliocentric velocity of the host galaxy (658 km s^{-1}; Table 1) using the DOPCOR task.

3. DISTANCE AND EXTINCTION

We adopt a distance of 9.57 ± 0.70 Mpc, which is a mean value of four different distance estimation techniques used for NGC 0628, viz., 9.91 Mpc applying the Standard Candle Method (SCM) to SN 2003gd by Olivares et al. (2010); 10.19 Mpc using the Tully–Fisher method (HyperLeda);[12] 9.59 Mpc using the brightest supergiant distance estimate by Hendry et al. (2005); and planetary nebula luminosity function distance 8.59 Mpc (Herrmann et al. 2008). Although for each of these methods a number of distance estimates exist in the literature, we tried to select only the most recent estimates. Richmond (2014) estimated a distance of 9.1 ± 0.4 Mpc by applying the Expanding Photosphere Method to SN 2013ej, which we find consistent with what we adopted.

One of the most reliable and well-accepted methods for SN line-of-sight reddening estimation is using the Na I D absorption feature. The equivalent width (EW) of the Na I D doublet ($\lambda\lambda$ 5890, 5896) is found to be correlated with the reddening, estimated from the tail color curves of SNe Ia (Barbon et al. 1990; Turatto et al. 2003). However, Poznanski et al. (2011) suggested that although Na I D EW is weakly correlated with $E(B-V)$, the EWs estimated from low-resolution spectra are a bad estimator of $E(B-V)$. Poznanski et al. (2012) used a larger sample of data and presented a more precise and rather different functional form of the correlation than what was derived earlier. Our high-resolution echelle spectra at 79.5 days provided an excellent opportunity to investigate the line-of-sight extinction.

The resolved Na I D doublet for the Milky Way is clearly visible in the high-resolution spectra (recorded on 79.5 days) as shown in Figure 2, whereas no impression of Na I D for NGC 0628 is detected at the expected redshifted position relative to

[11] http://swift.gsfc.nasa.gov/docs/swift/sne/swift_sn.html

[12] http://leda.univ-lyon1.fr/

Table 2
Eight Local Standards in the Field of SN 2013ej with Corresponding Coordinates (α, δ) and Calibrated Magnitudes in *UBVRI*. Errors Quoted Here Include Both Photometric and Calibration Errors

Star ID	α_{J2000} (h m s)	δ_{J2000} (° ′ ″)	U (mag)	B (mag)	V (mag)	R (mag)	I (mag)
A	1:36:57.9	+15:51:19.4	16.773 ± 0.0325	16.867 ± 0.0259	16.297 ± 0.0193	15.939 ± 0.0163	15.567 ± 0.0207
B	1:36:23.0	+15:47:45.3	15.102 ± 0.0289	15.109 ± 0.0302	14.580 ± 0.0234	14.253 ± 0.0183	13.888 ± 0.0260
C	1:36:50.4	+15:40:01.9	16.588 ± 0.0318	16.525 ± 0.0277	15.798 ± 0.0200	15.372 ± 0.0157	14.925 ± 0.0187
D	1:36:52.7	+15:40:39.4	14.811 ± 0.0318	14.561 ± 0.0265	13.817 ± 0.0184	13.384 ± 0.0167	12.976 ± 0.0196
E	1:37:03.4	+15:41:39.2	17.140 ± 0.0386	17.064 ± 0.0251	16.407 ± 0.0200	16.008 ± 0.0160	15.601 ± 0.0206
F	1:37:09.0	+15:41:20.4	18.804 ± 0.1537	17.800 ± 0.0282	16.769 ± 0.0249	16.146 ± 0.0167	15.583 ± 0.0205
G	1:36:57.6	+15:46:22.7	13.934 ± 0.0272	13.756 ± 0.0219	12.991 ± 0.0160	12.555 ± 0.0161	12.155 ± 0.0240
H	1:37:09.0	+15:48:00.6	16.974 ± 0.0434	16.172 ± 0.0249	15.175 ± 0.0157	14.598 ± 0.0170	14.062 ± 0.0194

the Milky Way. This indicates that the reddening due to the host is negligible, and only Galactic reddening will contribute to the total line-of-sight extinction. A similar conclusion has also been inferred by Valenti et al. (2014) from their high-resolution spectra obtained at 31 days. Thus, we adopt a total $E(B-V) = 0.060 \pm 0.001$ mag, which is entirely due to Galactic reddening (Schlafly & Finkbeiner 2011), and assuming total-to-selective extinction at V band as $R_V = 3.1$, it translates into $A_V = 0.185 \pm 0.004$ mag.

4. LIGHT CURVE

4.1. Light-curve Evolution and Comparison

The optical light curves of SN 2013ej in *UBVRI* and six UVOT bands are shown in Figure 3. *UBVRI* photometric observations were done at 38 phases during 12–209 days (from plateau to nebular phase). The duration of the plateau phase is sparsely covered, while denser follow-up initiated after 68 days. The plateau phase lasted ∼85 days, with an average decline rate of 6.60, 3.57, 1.74, 1.07, and 0.74 mag $(100\ \mathrm{days})^{-1}$ in *UBVRI* bands, respectively. Since 95 days, the light curve declines very fast until 115 days, after which it settles to a relatively slow declining nebular phase. During this phase, the decline rates for *UBVRI* bands are 0.98, 1.22, 1.53, 1.42, and 1.55 mag $(100\ \mathrm{days})^{-1}$, respectively.

SN 2013ej has been also observed by *Swift* UVOT at 35 phases during 7 to 139 days. The UVOT *UV* band light curves decline steeply during the first 30 days at a rate of 0.182, 0.213, and 0.262 mag day^{-1} in *uvw*1, *uvw*2, and *uvm*2 bands, respectively, thereafter settling into a slow declining phase until it reaches the end of the plateau.

SN 2013ej experiences a steeper plateau decline than that observed for SN 1999em (Leonard et al. 2002c), SN 1999gi (Leonard et al. 2002b), SN 2012aw (Bose et al. 2013), and SN 2013ab (Bose et al. 2015). For example, the SN 2012aw plateau declines at a rate of 5.60, 1.74, and 0.55 mag $(100\ \mathrm{days})^{-1}$ in *UBV* bands; similarly for SN 2013ab, decline rates in *UBVRI* are 7.60, 2.72, 0.92, 0.59, and 0.30 mag $(100\ \mathrm{days})^{-1}$ and 0.169, 0.236, 0.257 mag day^{-1} in UVOT *uvw*1, *uvw*2, and *uvm*2 bands (during the first 30 days).

The absolute V-band (M_V) light curve of SN 2013ej is plotted in Figure 4 and is compared with other well-studied SNe II (after correcting for extinction and distance). In Table 5 we list the plateau slope of all compared Type II events. The comparison shows that the decline rate of SN 2013ej during this phase is highest (1.74 mag $(100\ \mathrm{days})^{-1}$) among most other SNe, except three SNe IIL SN 1980 K, SN 2000dc, and SN 2013by, where SN 1980 is among the very first observed prototypical Type IIL event. The early plateau (<40 days) light curve of SN 2013ej is identical to that of SN 2009bw. However, unlike most other SNe IIP, e.g., SN 2009bw and SN 2013ab, which become flatter during the late plateau, SN 2013ej continues to decline almost at a steady rate until the end of the plateau (∼85 days). The mid-plateau $M_V = -14.7$ mag for SN 2013ej, which places it in the class of normal luminous Type II events. SN 2013ej is comparable with fast-declining and short-plateau SNe in the sample of Anderson et al. (2014b). Following the plateau phase, V-band light drops very fast to reach the slow-declining nebular phase (1.53 mag $(100\ \mathrm{days})^{-1}$), which is powered by the radioactive decay of ^{56}Co to ^{56}Fe. The fall of M_V during the plateau-nebular transition is ∼2.4 mag, which is on the higher side of the compared events. The closest comparison is SN 2009bw and SN 2012 A, which exhibit a drop of ∼2.4 and ∼2.5 mag, respectively. This also indicates a low amount of ^{56}Ni mass synthesized during the explosion, which we shall further discuss in the next section.

Swift UVOT absolute magnitude light curves of SN 2013ej are shown in Figure 5 and compared with other well-observed SNe II. The sample is selected in such a way that SNe have at least a month of observations. Most SNe are not followed for more than a month by *Swift*, mainly because of the large distances or high extinction values. However, both these factors work in favor of SN 2013ej, making it possible to have about 4 months of observations. Moreover, with the location of the SN being in the outskirts of a spiral arm of NGC 0628, the background flux contamination is also negligible. The comparison shows that the SN 2013ej UV light curves are identical to SN 2012aw. SN 2013ej also shows a similar UV-plateau trend as observed in SN 2012aw (Bayless et al. 2013), which is expected but rarely detected for SNe IIP/L.

Broadband color provides important information to study the temporal evolution of the SN envelope. In Figure 6, we plot the intrinsic colors $U-B$, $B-V$, $V-R$, and $V-I$ for SN 2013ej and compare its evolution with Type II-pec SN 1987 A and SNe IIP SN 1999em, SN 2004et, SN 2012aw, and SN 2013ab. All the colors show a generic signature of fast cooling ejecta until the end of the plateau (∼110 days). With the start of the nebular phase it continues to cool at a much slower rate in $V-I$ and $V-R$ colors, whereas $U-V$ and $B-V$ show a bluer trend. This is because, as the SN enters the nebular phase, the ejecta become depleted of free electrons, thereby making the envelope optically thin and so unable to thermalize the photons from radioactive decay of ^{56}Co to ^{56}Fe.

Table 3
Photometric Evolution of SN 2013ej. Errors Denote 1σ Uncertainty

UBVRI Photometry

UT Date (yyyy mm dd)	JD 2,456,000+	Phase[a] (day)	*U* (mag)	*B* (mag)	*V* (mag)	*R* (mag)	*I* (mag)	Tel[b]
2013 Aug 04.82	509.32	12.02	12.026 ± 0.061	12.633 ± 0.020	12.612 ± 0.013	12.434 ± 0.017	12.349 ± 0.018	HCT
2013 Aug 31.93	536.43	39.13	14.576 ± 0.251	14.208 ± 0.020	13.125 ± 0.011	12.670 ± 0.015	12.436 ± 0.011	HCT
2013 Sep 29.77	565.27	67.97	16.088 ± 0.027	14.991 ± 0.020	13.569 ± 0.012	13.056 ± 0.016	12.750 ± 0.016	HCT
2013 Sep 30.72	566.22	68.92	16.207 ± 0.109	14.956 ± 0.020	13.595 ± 0.008	12.992 ± 0.015	12.741 ± 0.016	ST
2013 Oct 02.87	568.37	71.07	16.223 ± 0.028	15.017 ± 0.020	13.640 ± 0.012	13.053 ± 0.015	12.750 ± 0.017	HCT
2013 Oct 13.70	579.20	81.90	16.823 ± 0.054	15.291 ± 0.015	13.864 ± 0.010	13.222 ± 0.017	⋯	ST
2013 Oct 15.85	581.35	84.05	17.026 ± 0.061	15.365 ± 0.021	13.884 ± 0.012	13.273 ± 0.011	12.978 ± 0.017	ST
2013 Oct 16.71	582.21	84.91	17.036 ± 0.089	15.406 ± 0.013	13.939 ± 0.010	13.288 ± 0.018	12.986 ± 0.025	ST
2013 Oct 21.73	587.23	89.93	17.292 ± 0.057	15.611 ± 0.017	14.126 ± 0.017	13.446 ± 0.016	13.147 ± 0.018	ST
2013 Oct 24.70	590.20	92.90	17.405 ± 0.035	15.743 ± 0.016	14.233 ± 0.021	13.540 ± 0.014	13.253 ± 0.014	ST
2013 Oct 25.72	591.22	93.92	17.365 ± 0.023	15.732 ± 0.014	14.340 ± 0.008	13.592 ± 0.011	13.322 ± 0.011	DFOT
2013 Oct 26.74	592.24	94.94	17.442 ± 0.020	15.795 ± 0.014	14.431 ± 0.007	13.672 ± 0.010	13.384 ± 0.011	DFOT
2013 Oct 27.76	593.26	95.96	17.515 ± 0.033	15.985 ± 0.022	14.453 ± 0.016	13.750 ± 0.016	13.447 ± 0.021	ST
2013 Nov 09.63	606.13	108.83	18.440 ± 0.039	17.611 ± 0.015	16.108 ± 0.012	15.144 ± 0.015	14.783 ± 0.016	HCT
2013 Nov 11.72	608.22	110.92	18.655 ± 0.106	17.725 ± 0.020	16.358 ± 0.012	15.357 ± 0.016	14.978 ± 0.016	ST
2013 Nov 12.67	609.17	111.87	⋯	17.700 ± 0.021	16.379 ± 0.014	15.358 ± 0.017	15.004 ± 0.014	ST
2013 Nov 14.65	611.15	113.85	⋯	17.764 ± 0.031	16.405 ± 0.011	15.402 ± 0.010	15.031 ± 0.013	ST
2013 Nov 19.69	616.19	118.89	18.515 ± 0.133	17.865 ± 0.023	16.493 ± 0.015	15.480 ± 0.016	15.133 ± 0.019	ST
2013 Nov 23.69	620.19	122.89	19.144 ± 0.408	17.945 ± 0.021	16.533 ± 0.009	15.529 ± 0.010	15.203 ± 0.011	ST
2013 Nov 24.62	621.12	123.82	18.973 ± 0.128	17.911 ± 0.019	16.552 ± 0.012	15.544 ± 0.015	15.205 ± 0.016	ST
2013 Dec 06.72	633.22	135.92	19.292 ± 0.171	18.113 ± 0.028	16.771 ± 0.014	15.719 ± 0.016	15.420 ± 0.017	ST
2013 Dec 08.73	635.23	137.93	19.286 ± 0.175	18.139 ± 0.018	16.815 ± 0.017	15.766 ± 0.022	15.486 ± 0.024	ST
2013 Dec 09.69	636.19	138.89	⋯	18.167 ± 0.022	16.832 ± 0.011	15.779 ± 0.017	15.488 ± 0.017	ST
2013 Dec 10.61	637.11	139.81	⋯	18.209 ± 0.034	16.863 ± 0.019	15.796 ± 0.020	15.490 ± 0.022	ST
2013 Dec 14.74	641.24	143.94	⋯	18.015 ± 0.093	16.892 ± 0.034	15.856 ± 0.020	15.597 ± 0.023	ST
2013 Dec 15.63	642.13	144.83	⋯	18.223 ± 0.041	16.974 ± 0.019	15.914 ± 0.025	15.603 ± 0.026	ST
2013 Dec 16.70	643.20	145.90	⋯	18.109 ± 0.053	16.943 ± 0.025	15.903 ± 0.019	15.596 ± 0.126	ST
2013 Dec 19.61	646.11	148.81	⋯	18.249 ± 0.043	17.009 ± 0.015	15.932 ± 0.019	15.661 ± 0.023	ST
2013 Dec 24.62	651.12	153.82	19.474 ± 0.061	18.265 ± 0.027	17.138 ± 0.014	16.003 ± 0.015	15.743 ± 0.016	ST
2013 Dec 25.66	652.16	154.86	⋯	18.321 ± 0.016	17.101 ± 0.010	16.012 ± 0.009	15.722 ± 0.012	ST,DFOT
2013 Dec 28.62	655.12	157.82	19.368 ± 0.058	18.325 ± 0.019	17.161 ± 0.009	16.041 ± 0.015	15.760 ± 0.016	DFOT
2013 Dec 29.59	656.09	158.79	19.436 ± 0.060	18.315 ± 0.024	17.180 ± 0.011	16.061 ± 0.010	15.791 ± 0.011	DFOT
2014 Jan 19.62	677.12	179.82	⋯	18.676 ± 0.025	17.458 ± 0.011	16.370 ± 0.014	16.128 ± 0.015	ST
2014 Jan 25.62	683.12	185.82	19.703 ± 0.071	18.638 ± 0.013	17.526 ± 0.009	16.424 ± 0.011	16.164 ± 0.012	DFOT
2014 Jan 30.62	688.12	190.82	19.797 ± 0.596	18.785 ± 0.027	17.602 ± 0.014	16.501 ± 0.013	16.282 ± 0.015	ST
2014 Jan 31.58	689.08	191.78	⋯	18.787 ± 0.030	17.618 ± 0.019	16.522 ± 0.017	16.273 ± 0.025	ST
2014 Feb 02.62	691.12	193.82	⋯	18.813 ± 0.035	17.623 ± 0.031	16.546 ± 0.020	16.323 ± 0.024	ST
2014 Feb 17.59	706.09	208.79	⋯	19.218 ± 0.079	17.814 ± 0.022	16.682 ± 0.012	16.470 ± 0.017	ST

Swift UVOT Photometry

UT Date (yyyy mm dd)	JD 2,456,000+	Phase[a] (day)	*uvw2* (mag)	*uvm2* (mag)	*uvw1* (mag)	*uvu* (mag)	*uvb* (mag)	*uvv* (mag)	Tel[b] /Inst
2013 Jul 30.98	504.48	7.18	12.369 ± 0.040	12.023 ± 0.040	11.711 ± 0.039	⋯	⋯	12.689 ± 0.042	*Swift*
2013 Jul 31.50	505.00	7.70	12.455 ± 0.040	12.097 ± 0.040	11.755 ± 0.039	⋯	⋯	12.614 ± 0.040	*Swift*

Table 3
(Continued)

Swift UVOT Photometry									
UT Date (yyyy mm dd)	JD 2,456,000+	Phase[a] (day)	*uvw2* (mag)	*uvm2* (mag)	*uvw1* (mag)	*uvu* (mag)	*uvb* (mag)	*uvv* (mag)	Tel[b] /Inst
2013 Jul 31.83	505.33	8.03	12.577 ± 0.035	12.204 ± 0.033	11.814 ± 0.032	⋯	⋯	⋯	*Swift*
2013 Aug 03.06	507.56	10.26	13.044 ± 0.037	12.695 ± 0.041	⋯	11.675 ± 0.029	12.619 ± 0.029	⋯	*Swift*
2013 Aug 03.18	507.68	10.38	13.056 ± 0.035	⋯	⋯	⋯	12.622 ± 0.029	⋯	*Swift*
2013 Aug 04.85	509.35	12.05	13.374 ± 0.040	13.155 ± 0.053	⋯	11.812 ± 0.029	12.608 ± 0.029	⋯	*Swift*
2013 Aug 04.98	509.48	12.18	13.385 ± 0.037	⋯	⋯	⋯	⋯	⋯	*Swift*
2013 Aug 07.24	511.74	14.44	13.907 ± 0.041	⋯	12.948 ± 0.042	⋯	⋯	⋯	*Swift*
2013 Aug 07.55	512.05	14.75	13.968 ± 0.050	⋯	⋯	⋯	⋯	⋯	*Swift*
2013 Aug 08.02	512.52	15.22	14.039 ± 0.052	14.058 ± 0.070	13.131 ± 0.038	12.185 ± 0.031	12.749 ± 0.029	12.477 ± 0.030	*Swift*
2013 Aug 08.22	512.72	15.42	14.126 ± 0.045	⋯	⋯	12.266 ± 0.029	⋯	⋯	*Swift*
2013 Aug 09.25	513.75	16.45	14.387 ± 0.055	14.305 ± 0.112	13.379 ± 0.041	12.333 ± 0.029	12.906 ± 0.029	12.535 ± 0.031	*Swift*
2013 Aug 09.31	513.81	16.51	⋯	14.406 ± 0.065	⋯	⋯	⋯	⋯	*Swift*
2013 Aug 11.78	516.28	18.98	15.210 ± 0.118	15.114 ± 0.109	13.907 ± 0.052	12.659 ± 0.029	12.983 ± 0.029	12.581 ± 0.031	*Swift*
2013 Aug 13.85	518.35	21.05	15.652 ± 0.082	15.964 ± 0.068	14.446 ± 0.059	12.982 ± 0.031	13.109 ± 0.029	12.599 ± 0.032	*Swift*
2013 Aug 15.00	520.50	23.20	16.209 ± 0.090	⋯	14.905 ± 0.069	13.308 ± 0.033	13.221 ± 0.030	12.573 ± 0.032	*Swift*
2013 Aug 17.65	522.15	24.85	16.588 ± 0.098	17.109 ± 0.195	15.201 ± 0.072	13.602 ± 0.035	13.293 ± 0.030	12.656 ± 0.032	*Swift*
2013 Aug 19.73	524.23	26.93	16.824 ± 0.105	17.554 ± 0.221	15.493 ± 0.076	13.964 ± 0.039	13.476 ± 0.030	12.692 ± 0.032	*Swift*
2013 Aug 22.54	527.04	29.74	17.245 ± 0.120	18.047 ± 0.250	15.890 ± 0.075	14.338 ± 0.045	13.663 ± 0.032	12.816 ± 0.033	*Swift*
2013 Aug 23.14	527.64	30.34	17.170 ± 0.117	⋯	15.866 ± 0.083	14.366 ± 0.045	13.627 ± 0.031	12.892 ± 0.034	*Swift*
2013 Aug 27.74	532.24	34.94	17.746 ± 0.146	18.569 ± 0.214	16.356 ± 0.095	14.844 ± 0.058	13.915 ± 0.033	12.965 ± 0.034	*Swift*
2013 Sep 06.16	541.66	44.36	18.133 ± 0.124	19.137 ± 0.190	16.793 ± 0.084	15.573 ± 0.067	⋯	⋯	*Swift*
2013 Sep 06.41	541.91	44.61	⋯	⋯	⋯	15.674 ± 0.087	14.367 ± 0.036	13.231 ± 0.035	*Swift*
2013 Sep 16.71	552.21	54.91	18.687 ± 0.158	19.486 ± 0.236	17.292 ± 0.096	16.229 ± 0.090	14.750 ± 0.039	13.470 ± 0.038	*Swift*
2013 Sep 26.45	561.95	64.65	18.793 ± 0.166	⋯	17.562 ± 0.123	16.585 ± 0.128	14.922 ± 0.042	13.604 ± 0.039	*Swift*
2013 Oct 06.88	572.38	75.08	19.241 ± 0.231	19.883 ± 0.333	17.919 ± 0.133	17.055 ± 0.094	⋯	⋯	*Swift*
2013 Oct 16.77	582.27	84.97	19.294 ± 0.247	⋯	18.127 ± 0.170	17.286 ± 0.164	15.464 ± 0.055	14.029 ± 0.045	*Swift*
2013 Oct 26.95	592.45	95.15	⋯	⋯	18.248 ± 0.190	17.514 ± 0.171	⋯	⋯	*Swift*
2013 Nov 06.16	602.66	105.36	⋯	⋯	⋯	18.774 ± 0.304	⋯	⋯	*Swift*
2013 Nov 13.21	609.71	112.41	⋯	⋯	19.523 ± 0.351	19.058 ± 0.306	⋯	⋯	*Swift*
2013 Nov 13.68	610.18	112.88	⋯	⋯	⋯	18.816 ± 0.263	17.974 ± 0.210	16.512 ± 0.148	*Swift*
2013 Nov 20.43	616.93	119.63	⋯	⋯	⋯	18.977 ± 0.214	17.889 ± 0.090	16.718 ± 0.080	*Swift*
2013 Nov 25.40	621.90	124.60	⋯	⋯	⋯	19.162 ± 0.323	⋯	⋯	*Swift*
2013 Nov 30.43	626.93	129.63	⋯	⋯	19.726 ± 0.313	19.342 ± 0.280	18.155 ± 0.101	16.834 ± 0.082	*Swift*
2013 Dec 09.75	636.25	138.95	⋯	⋯	19.807 ± 0.327	19.343 ± 0.274	18.196 ± 0.102	16.928 ± 0.085	*Swift*

Notes. Data observed within 5 hr are represented under single-epoch observation.
[a] With reference to the explosion epoch JD 2,456,497.30.
[b] ST: 104 cm Sampurnanand Telescope, ARIES, India; DFOT: 130 cm Devasthal Fast Optical Telescope, ARIES, India; HCT: 2 m Himalyan Chandra Telescope, Hanle, India; *Swift*: *Swift* UVOT.

Table 4
Summary of Spectroscopic Observations of SN 2013ej. The Spectral Observations are Made at 10 Phases during 12 to 125 days

UT Date (yy/mm/dd.dd)	JD 2,456,000+	Phase[a] (days)	Telescope[c]	Range[b] μm	Exposure (s)
2013 Aug 04.86	509.36	12.1	HCT	0.38–0.68	900
2013 Aug 27.76	532.26	35.0	HCT	0.38–0.68	1200
			HCT	0.58–0.84	1200
2013 Sep 03.90	539.40	42.1	HCT	0.38–0.68	1500
			HCT	0.58–0.84	1500
2013 Sep 29.78	565.28	68.0	HCT	0.38–0.68	1800
			HCT	0.58–0.84	2400
2013 Oct 02.89	568.39	71.1	HCT	0.38–0.68	1500
			HCT	0.58–0.84	1500
2013 Oct 11.28	576.78	79.5	APO	0.32–1.00	1200
2013 Oct 27.87	593.37	96.1	HCT	0.38–0.68	2400
2013 Oct 28.79	594.29	97.0	HCT	0.58–0.84	2400
2013 Nov 09.65	606.15	108.9	HCT	0.38–0.68	2100
			HCT	0.58–0.84	3900
2013 Nov 25.75	622.25	125.0	HCT	0.38–0.68	2400
	…	…	HCT	0.58–0.84	2400

Notes.
[a] With reference to the adopted explosion time JD 2,456,497.30.
[b] For transmission $\geqslant$50%.
[c] HCT: HFOSC on 2 m Himalyan Chandra Telescope, India; APO: Echelle spectrograph on 3.5 m ARC telescope at Apache Point Observatory, USA.
[d] At 0.6 μm.

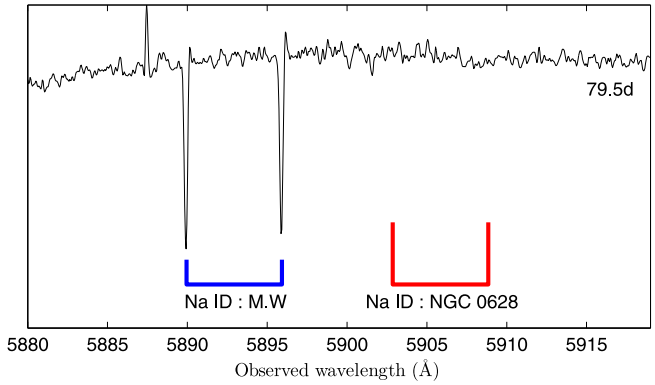

Figure 2. Echelle spectra at 79.5 days showing the Na I D doublet for the Milky Way, while no impression for NGC 0628 is detected.

4.2. Bolometric Light Curve

We compute the pseudo-bolometric luminosities following the method described in Bose et al. (2013), which include SED integration over the semi-deconvolved photometric fluxes after correcting for extinction and distance. SN bolometric luminosities during early phases ($\leqslant$30 days) are dominated by UV fluxes, while after mid-plateau ($\sim$50 days) UV contribution becomes insignificant as compared to the optical counterpart (e.g., as seen in SN 2012aw and SN 2013ab; Bose et al. 2013, 2015). Similarly, during late phases $>$100 days, near-infrared becomes dominant over optical fluxes. However, during most of the light-curve evolution, optical fluxes still provide significant contribution. We compute pseudo-bolometric luminosities in the wavelength range of *U* to *I* band (3335–8750 Å). We also computed a UV–optical pseudo-bolometric light curve with wavelength starting from the *uvw2* band (wavelength range of 1606–8750 Å). The UV contribution enhances the luminosity significantly during early phases, whereas it is almost negligible after mid-plateau.

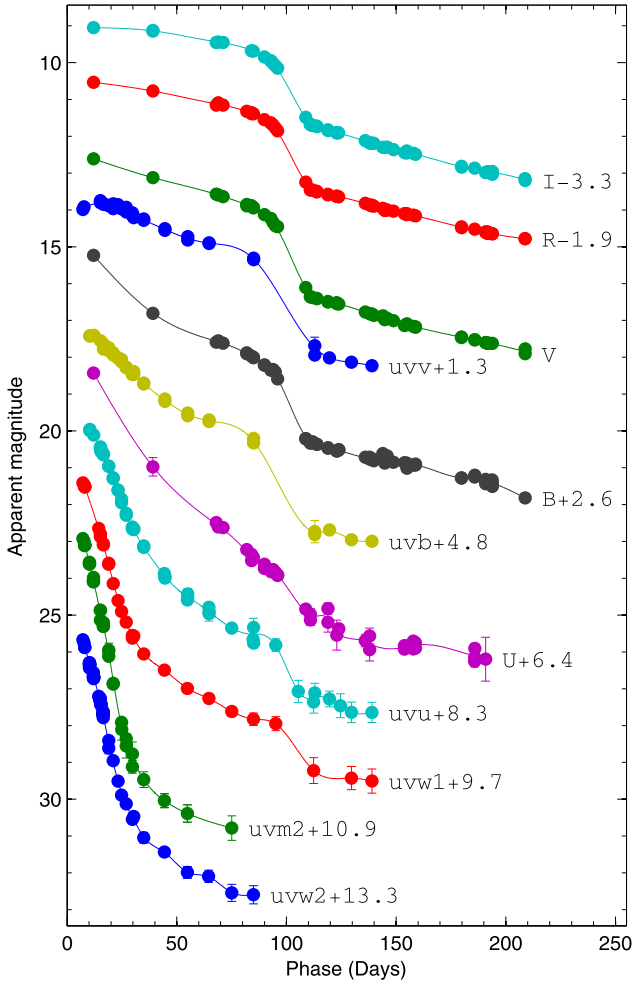

Figure 3. Photometric light curves in Johnson–Cousins *UBVRI* and *Swift* UVOT bands. The light curves are vertically shifted for clarity. The line joining the data points of light curves is for visualization purposes only.

In Figure 7, we plot a pseudo-bolometric light curve for SN 2013ej and compare it with other SN light curves computed using the same technique. We also include UV–optical bolometric light curves for SN 2012aw and SN 2013ab, along with SN 2013ej for comparison. Although the UV–optical light curve is initially brighter than the optical light curve, they completely coincide by the end of the plateau phase (85 days). It is evident from the comparison that SN 2013ej experienced a steep decline during the plateau phase, but with a much shorter duration. This is consistent with the anticorrelation observed between plateau slope and duration for SNe II (Blinnikov & Bartunov 1993; Anderson et al. 2014b). The UV–optical bolometric light decreases by 0.83 dex during the plateau phase (from 12 to 85 days), followed by an even faster drop by 0.76 dex in a short duration of 21 days (from 90 to 111 days). Thereafter, the SN settles in a slow-declining nebular phase. The tail luminosities are significantly lower than other normal-luminosity IIP events, e.g., SN 2013ej luminosities are lower

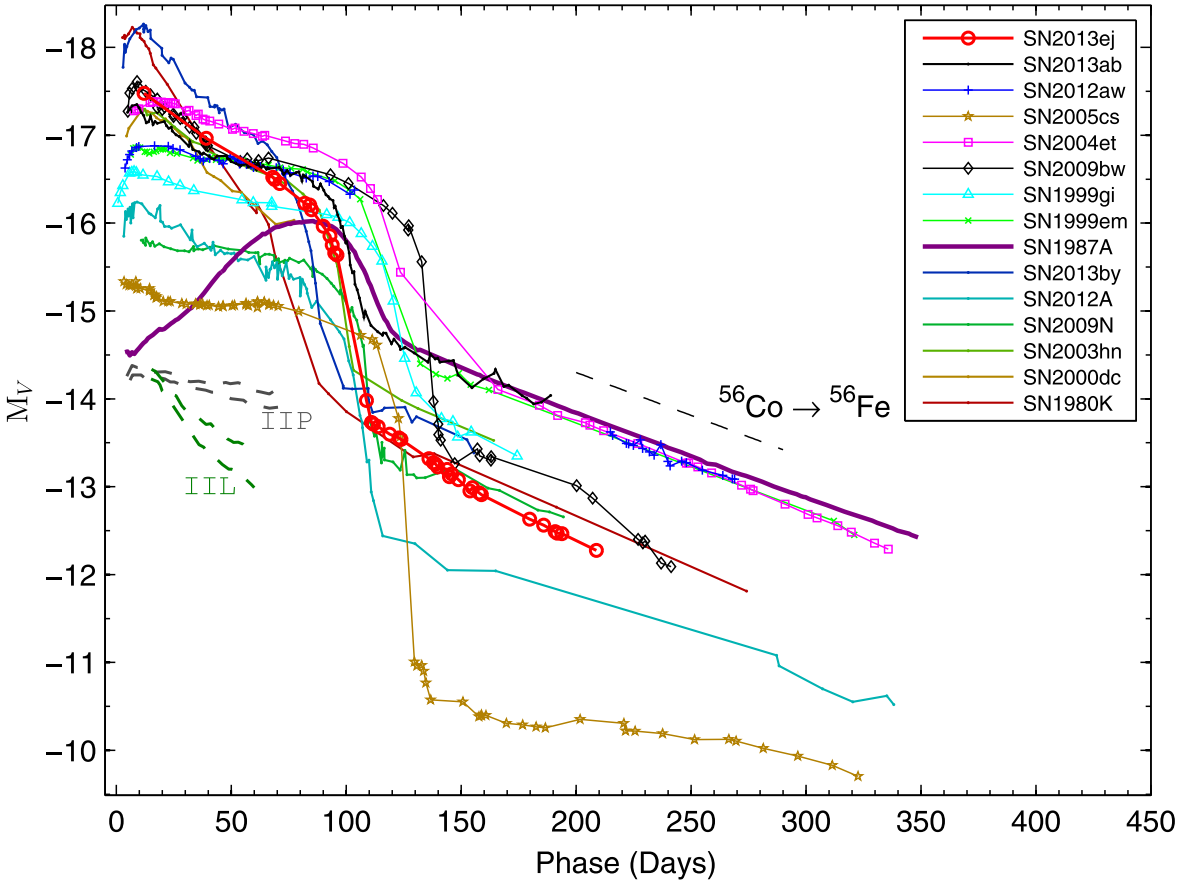

Figure 4. M_V light curve of SN 2013ej compared with other SNe II. The exponential decline of the tail light curve following the radioactive decay law for ^{56}Co → ^{56}Fe is shown with a dashed line. On the bottom left side, the pair of dotted lines in gray and green represent the slope range for SN IIP and IIL templates, respectively, as given by Faran et al. (2014). The adopted explosion time in JD –2,400,000, distance in Mpc, $E(B-V)$ in mag, and the reference for observed V-band magnitude, respectively, are as follows: SN 1980 K—44,540.5, 5.5, 0.30; Barbon et al. (1982), NED database; SN 1987 A—46,849.8, 0.05, 0.16; Hamuy & Suntzeff (1990); SN 1999em—51,475.6, 11.7, 0.10; Leonard et al. (2002a); Elmhamdi et al. (2003); SN 1999gi—51,522.3, 13.0, 0.21; Leonard et al. (2002b); SN 2000dc—51,762.4, 49.0, 0.07; Faran et al. (2014), NED database; SN 2003hn—52,866.5, 17.0, 0.19; Krisciunas et al. (2009); Anderson et al. (2014b); SN 2004et—53,270.5, 5.4, 0.41; Sahu et al. (2006); SN 2005cs—53,549.0, 7.8, 0.11; Pastorello et al. (2009); SN 2009 N—54,848.1, 21.6, 0.13; Takáts et al. (2014); SN 2009bw—54,916.5, 20.2, 0.31; Inserra et al. (2012); SN 2012 A—55,933.5, 9.8, 0.04; Tomasella et al. (2013); SN 2012aw—56,002.6, 9.9, 0.07; Bose et al. (2013); SN 2013ab—56,340.0, 24.0, 0.04; Bose et al. (2015); SN 2013by—56,404.0, 14.8, 0.19; Valenti et al. (2015).

by ∼0.5 dex (at 200 days) than that of SNe II SN 1987 A, SN 1999em, SN 2004et, and SN 2012aw, but higher than subluminous events like SN 2005cs. Another noticeable dissimilarity of the tail light curve is its high decline rate. The SN 2013ej tail luminosity declines at a rate of 0.55 dex $(100\,\mathrm{days})^{-1}$, which is much higher than that expected from radioactive decay of ^{56}Co to ^{56}Fe. This is possibly because of inefficient gamma-ray trapping in the ejecta and thus incomplete thermalization of the photons. We shall further explore this in Section 7 in context of modeling the light curve.

4.3. Mass of Nickel

During the explosive nucleosynthesis of silicon and oxygen, at the time of shock breakout in CCSNe, radioactive ^{56}Ni is produced. The nebular phase light curve is mainly powered by the radioactive decay of ^{56}Ni to ^{56}Co and ^{56}Co to ^{56}Fe with half-life times of 6.1 and 77.1 days, respectively, emitting γ-rays and positrons. Thus, the tail luminosity will be proportional to the amount of radioactive ^{56}Ni synthesized at the time of explosion. We determine the mass of ^{56}Ni using the following two methods.

For SN 1987 A, one of the most well-studied and well-observed events, the mass of ^{56}Ni produced in the explosion has been estimated quite accurately, to be $0.075 \pm 0.005\,M_\odot$ (Arnett 1996). By comparing the tail luminosities of SN 2013ej and SN 1987 A at similar phases, it is possible to estimate the ^{56}Ni mass for SN 2013ej. In principle, true bolometric luminosities (including UV, optical, and IR) are to be used for this purpose, which are available for SN 1987 A, whereas for SN 2013ej we have only UV and optical observations. Thus, in order to have uniformity in comparison, we used only the *UBVRI* bolometric luminosities for both SNe and computed using the same method and wavelength range. We estimate the tail *UBVRI* luminosity at 175 days, by making a linear fit over 155–195 days, to be $2.90 \pm 0.43 \times 10^{40}$ erg s^{-1}. Likewise, SN 1987 A luminosity is estimated to be $9.60 \pm 0.06 \times 10^{40}$ erg s^{-1} at similar phase. Thus, the ratio of SN 2013ej to SN 1987 A luminosity is 0.302 ± 0.044, which corresponds to a ^{56}Ni mass of $0.023 \pm 0.003\,M_\odot$ for SN 2013ej.

Assuming that the γ-photons emitted from radioactive decay of ^{56}Co thermalize the ejecta, ^{56}Ni mass can be independently estimated from the tail luminosity as described by Hamuy

Table 5
Parameters Estimated from the *V*-band Light Curve

SN Name	Plateau Slope[a] (mag (100 days)$^{-1}$)	Transition Drop[b] (mag)	Transition Time[c] (days)
SN1980K	3.63 ± 0.04	2.0 ± 0.04	37 ± 5
SN 2000dc	2.56 ± 0.06[d]	…	…
SN 2013by	2.01 ± 0.02	2.2 ± 0.03	19 ± 5
SN 2013ej	1.74 ± 0.08	2.4 ± 0.02	21 ± 3
SN 2003hn	1.41 ± 0.04	2.0 ± 0.04	19 ± 4
SN 2012A	1.12 ± 0.03	2.5 ± 0.02	23 ± 4
SN 2009bw	0.93 ± 0.04	2.4 ± 0.03	14 ± 3
SN 2004et	0.73 ± 0.02	2.1 ± 0.04	27 ± 6
SN 2013ab	0.54 ± 0.02	1.7 ± 0.02	25 ± 2
SN 2012aw	0.51 ± 0.02	…	…
SN 1999gi	0.47 ± 0.02	2.0 ± 0.02	29 ± 3
SN 2005cs	0.44 ± 0.03	4.0 ± 0.03	24 ± 3
SN 2009N	0.36 ± 0.03	2.0 ± 0.04	26 ± 3
SN 1999em	0.31 ± 0.02	1.9 ± 0.02	28 ± 4

Notes.
Objects are sorted in order of plateau slope.
[a] Plateau slope during the linear decline phase, starting after first minima until plateau end.
[b] Drop in magnitude during the plateau-to-nebular transition.
[c] Duration of plateau-to-nebular transition.
[d] Slope is calculated up to the available range of data, as plateau end is not observed.

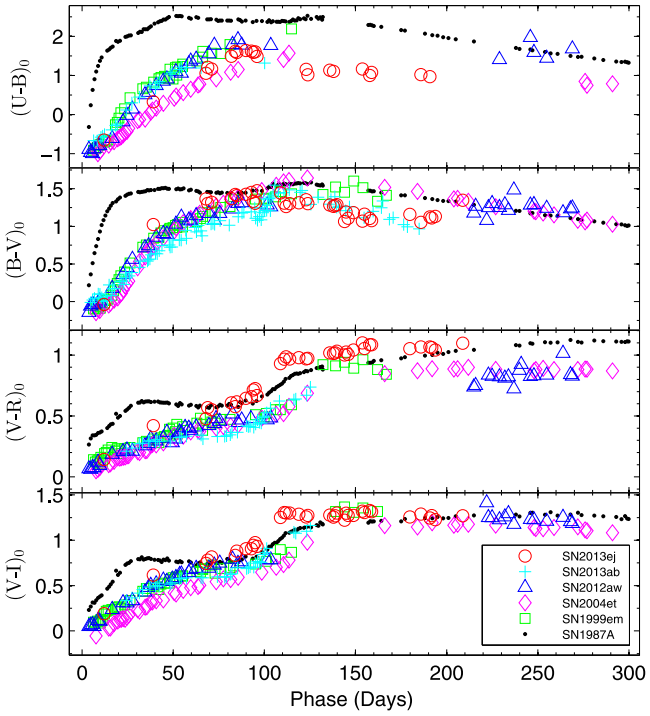

Figure 6. Intrinsic color evolution of SN 2013ej compared with other well-studied SNe IIP, SN 1987 A, SN 1999em, SN 2004et, SN 2012aw, and SN 2013ab. The references for the data are the same as in Figure 4.

(2003):

$$M_{\rm Ni} = 7.866 \times 10^{-44} \times L_t \exp\left[\frac{(t_t - t_0)/(1+z) - 6.1}{111.26}\right] M_\odot$$

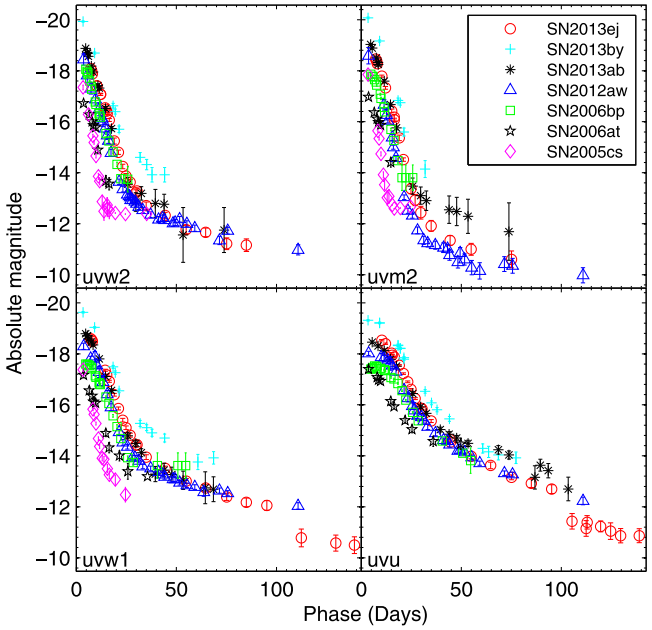

Figure 5. Comparison of the *Swift* UVOT UV absolute light curves of SN 2013ej, with other well-observed SNe II from UVOT. For the compared SNe, references for UVOT data, extinction, and distance are as follows: SN 2005cs —Brown et al. (2009); Pastorello et al. (2009); SN 2006at—Brown et al. (2009), distance 65 Mpc, $E(B-V)$= 0.031 mag (only Galactic reddening; Schlafly & Finkbeiner 2011); SN 2006bp—Dessart et al. (2008); SN 2012aw —Bayless et al. (2013); Bose et al. (2013); SN 2013ab—Bose et al. (2015); SN 2013by—Brown et al. (2014); Valenti et al. (2015). Some late data points for SN 2013ab with large errors have been omitted from the plot.

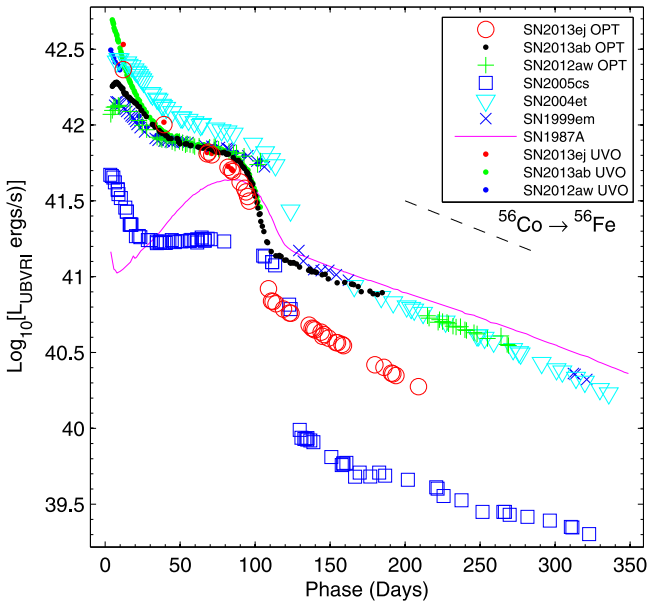

Figure 7. *UBVRI* bolometric light curve of SN 2013ej compared with other well-studied supernovae. Light curves with added UVOT UV contributions are also shown for SN 2013ej, SN 2013ab, and SN 2012aw (labeled as UVO). The adopted values of distances, reddening, and explosion time are the same as in Figure 4. The exponential decline of the tail light curve following the radioactive decay law is shown with a dashed line.

where t_0 is the explosion time, 6.1 days is the half-life time of ^{56}Ni, and 111.26 days is the *e*-folding time of the ^{56}Co decay. We compute tail luminosity L_t at 6 epochs within 153–185 days from the *V*-band data corrected for distance, extinction, and

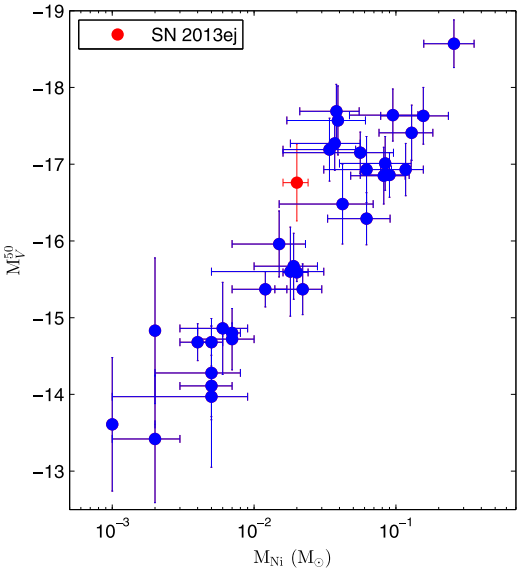

Figure 8. Plot of absolute *V*-band magnitude at 50 days vs. ^{56}Ni mass for 34 SNe II. Data taken from Hamuy (2003) and Spiro et al. (2014). The position of SN 2013ej on the correlation is shown with a filled red circle.

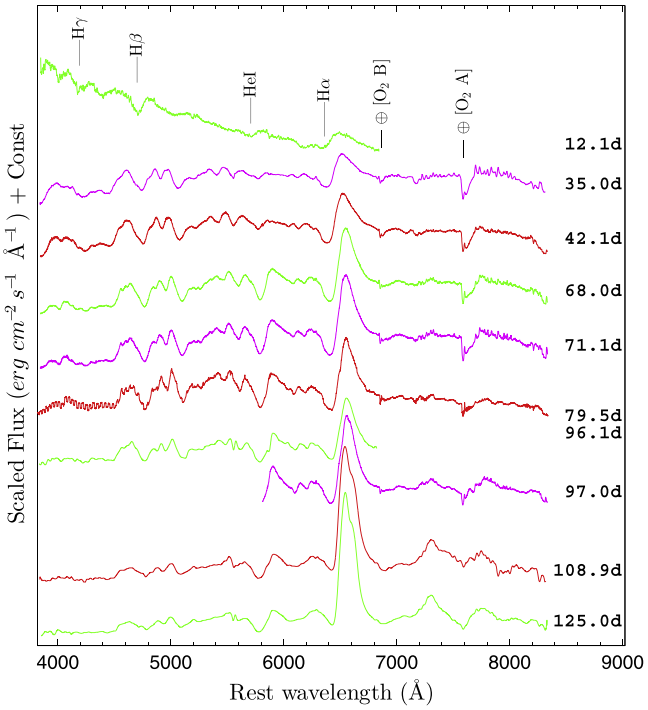

Figure 9. Redshift-corrected spectra of SN 2013ej are plotted for 10 phases during 12–125 days. The prominent P Cygni profiles of hydrogen (Hα, Hβ, Hγ) and helium (He I λ5876) are marked. The telluric absorption features of O_2 are marked with a $\oplus$ symbol. A portion of the spectra in the extreme blue or red ends have low signal-to-noise ratio. Individual spectra with overall low signal-to-noise ratio have been binned for better visualization.

bolometric correction factor of 0.26 ± 0.06 mag during the nebular phase (Hamuy 2003). The weighted mean value of L_t is found to be $5.45 \pm 0.35 \times 10^{40}$ erg s^{-1} corresponding to a mean phase of 170 days. This tail luminosity corresponds to a value of $M_{Ni} = 0.019 \pm 0.002\ M_\odot$.

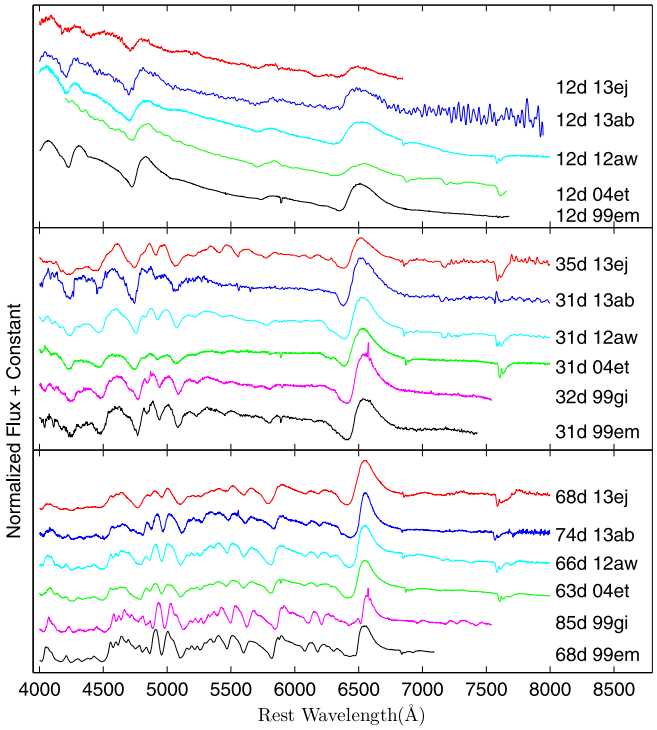

Figure 10. Comparison of early- (12 days) and plateau-phase (35 days, 68 days) spectra of SN 2013ej with other well-studied SNe IIP SN 1999em (Leonard et al. 2002a), SN 1999gi (Leonard et al. 2002b), SN 2004et (Sahu et al. 2006; Maguire et al. 2010), SN 2012aw (Bose et al. 2013), and SN 2013ab (Bose et al. 2015). All comparison spectra are corrected for extinction and redshift (adopted values are the same as in Figure 4).

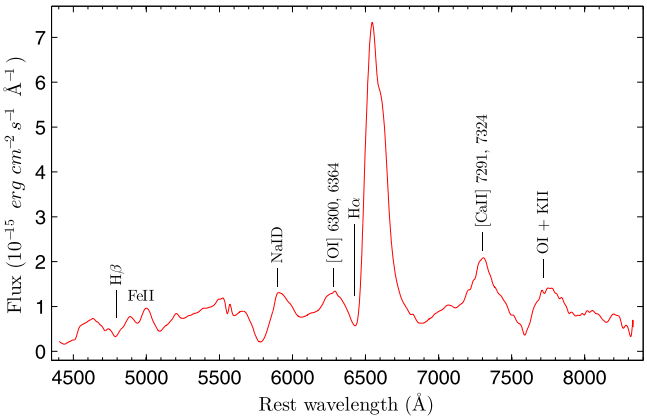

Figure 11. Nebular-phase spectrum of SN 2013ej at 125 days. Prominent emission and absorption features are marked and labeled.

We take the weighted mean of the estimated values from the above two methods and adopt a ^{56}Ni mass of 0.020 ± 0.002 $M_\odot$ for SN 2013ej.

Hamuy (2003) found a strong correlation between the ^{56}Ni mass and the mid-plateau (at 50 days) *V*-band absolute magnitude for SNe II, and this correlation was further confirmed by Spiro et al. (2014) specifically for low-luminosity events. Figure 8 shows the correlation of mid-plateau M_V versus ^{56}Ni mass for 34 events, including SN 2013ej. The SN lies within the scatter relation, but toward the lower mass range of ^{56}Ni than where most of the events cluster around (top right).

5. OPTICAL SPECTRA

5.1. Key Spectral Features

The spectroscopic evolution of SN 2013ej is presented in Figure 9. Preliminary identifications of spectral features have been done as per previously studied SNe IIP (e.g., Leonard et al. 2002a; Bose et al. 2013). The spectrum at 12 days shows broad Hα, Hβ, and He I features on top of a hot blue continuum. The 35-day spectrum shows a relatively flat continuum with well-developed features of Hα, Hβ, and Fe II along with blends of other heavier species like Ti II and Ba II. The He I line is no longer detectable; instead, Na I D features start to appear at a similar location. The spectra from 35 to 80 days represent the cooler photospheric phase, where the photosphere starts to penetrate deeper layers rich in heavier elements like Fe II and Sc II. During these phases, we see the emergence and development of various other heavy atomic lines and their blends such as Ti II, Ba II, Na I D, and Ca II. Figure 10 shows the comparison of three plateau-phase spectra, viz., 12, 35, and 68 days, with other well-studied SNe IIP at similar epochs. The comparison shows that the spectrum of SN 2013ej is broadly identical to others in terms of observable line features and their evolution. A notable feature during the early spectrum (12 days) is the dip on the bluer wing of Hα profiles near 6170 Å, which can be attributed to the Si II feature. Leonard et al. (2013) also identified this feature at ~9-day spectra of SN 2013ej; however, due to the unlikeliness of such a strong Si II feature at such early epochs, the possiblity of a non-standard red supergiant envelope or CSM interaction was suggested. However, such dips are detectable in 35- and 42-day spectra, which we identify as the Si II feature in SYNOW modeling.

The spectra at 96 and 97 days represent the plateau-nebular transition phase. Thereafter, spectra at 109 and 125 days represent the nebular phase, where the ejecta has become optically thin. These spectra show the emergence of some emission features from forbidden lines of [O I] $\lambda\lambda$6300, 6364 and [Ca II] $\lambda\lambda$7291, 7324, as well as previously evolved permitted lines of H I and the Na I λ5893 doublet (see Figure 11).

Gutiérrez et al. (2014) found correlations between Hα absorption-to-emission strengths and light-curve parameters, i.e., plateau slope and duration of optically thick phase. Following their selection criteria for choosing the phase of SN spectra, i.e., 10 days after start of recombination, we selected the 42-day spectrum as the closet available phase to the criteria. The Hα absorption-to-emission ratio of EWs for SN 2013ej is found to be 0.23 ± 0.02, the optically thick phase is ~85 days, and the *B*-band late-plateau (40–85 days) slope is ~0.27 mag $(100 \text{ days})^{-1}$. The correlation for optically thick phase duration is found to follow that presented by Gutiérrez et al. (2014). For the plateau slope, the correlation also holds true, but here SN 2013ej lies in the borderline position of the scattered relation. However, it may be noted that Hα profiles are possibly contaminated by high-velocity (HV) features, as we describe in the following sections, which may result in deviation from correlation.

5.2. SYNOW Modeling of Spectra

SN 2013ej spectra have been modeled with SYNOW[13] (Fisher et al. 1997, 1999; Branch et al. 2002) for line identification and its velocity estimation. SYNOW is a highly parametrized spectrum synthesis code that employs the Sobolev approximation to simplify radiation transfer equations assuming a spherically symmetric SN expanding homologously. The strength of the SYNOW code is its capability to reproduce P Cygni profiles simultaneously in synthetic spectra for a given set of atomic species and ionization states.

The applicability of SYNOW is well tested in various core-collapse SN studies (e.g., Inserra et al. 2012; Bose et al. 2013; Milisavljevic et al. 2013; Bose & Kumar 2014; Takáts et al. 2014; Marion et al. 2014) for velocity estimation and analysis of spectral lines.

To model the spectra, we tried various optical depth profiles (viz., Gaussian, exponential, and power law) with no significant difference among them; however, we find the exponential profile ($\tau \propto \exp[-v/v_e]$) marginally better suited to match the absorption trough of observed spectra, where v_e, the *e*-folding velocity, is a fitted parameter. While modeling spectra, H I lines are always dealt with as a detached scenario. This implies that the velocity of the hydrogen layer is significantly higher and is thus detached from the photospheric layer, close to which most heavier atomic lines form, as assumed in the SYNOW code. As a consequence of this, the Hα lines in synthetic spectra, which are highly detached, have flat-topped emissions with blueshifted absorption counterparts.

SN 2013ej spectra are dereddened and the approximate blackbody temperature is supplied in the model to match the spectral continuum. For the early spectrum (12 days), the local thermodynamic equilibrium (LTE) assumption holds, and thus SYNOW could fit the continuum well, whereas at later epochs it fails to fit properly. The set of atomic species incorporated to generate the synthetic model spectrum are H I, He I, Fe II, Ti II, Sc II, Ca II, Ba II, Na I, and Si II. The photospheric velocity $v_{\rm ph}$ is optimized to simultaneously fit the Fe II ($\lambda\lambda$4924, 5018, 5169) P Cygni profiles, and H I lines are treated as detached. The optical depths and optical depth profile parameters, which is the *e*-folding velocity, are varied for individual species to fit respective line profiles. In Figure 12 we show the model fit of the 71-day spectrum. Most of the observable spectral features are reproduced well and are identified in the figure.

Similarly, all spectra during 12–97 days are modeled with SYNOW. The model fits for Fe II ($\lambda\lambda$4924, 5018, 5169), Hβ, and Hα spectral sections are shown in Figure 13. The atomic species that are important to model these features are H I, Fe II, Ba II, Ti II, Sc II, and Na I. In addition to these, Si II is also used to model the dips in the blue wing of Hα P Cygni during 12–42 days. While modeling the Hα and Hβ profiles, SYNOW was unable to properly fit the broad and extended P Cygni absorption troughs with a single regular component. In order to fit these extended troughs, we invoke the HV component of H I. Although no separate dip is seen, possibly due to low spectral resolution and overlapping of broad P Cygni profiles, the HV component can well reproduce the observed features in the synthetic model spectrum. The implication and interpretation of these HV components are further discussed in Section 5.4. The SYNOW-derived velocities for Fe II, Hα, and Hβ lines and corresponding HV components are listed in Table 6. The nebular spectra during 109–125 days have not been modeled, primarily due to limitations of the LTE assumption of SYNOW, and also because nebular-phase spectra are dominated by emission lines rather than P Cygni profiles.

[13] https://c3.lbl.gov/es/#id22

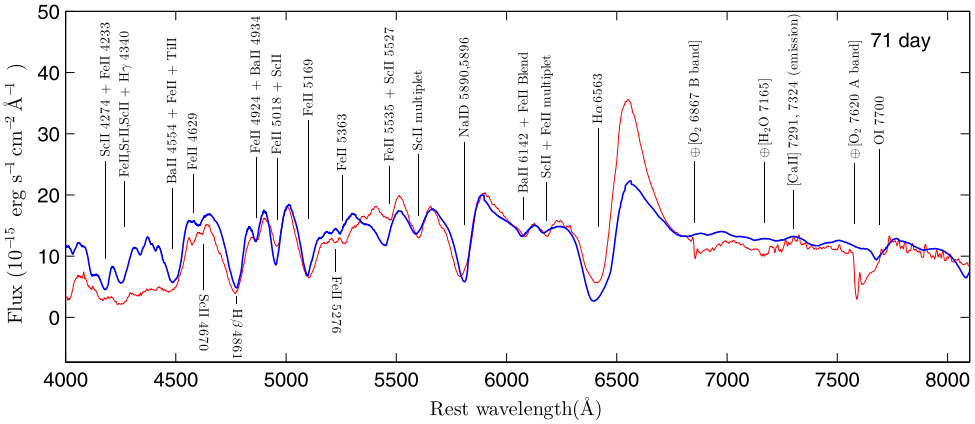

Figure 12. SYNOW modeling of the SN 2013ej spectrum at 71 days. The model spectrum is shown with a thick solid line (blue), while the observed one is shown with a thin solid line (red). Observed fluxes are corrected for extinction.

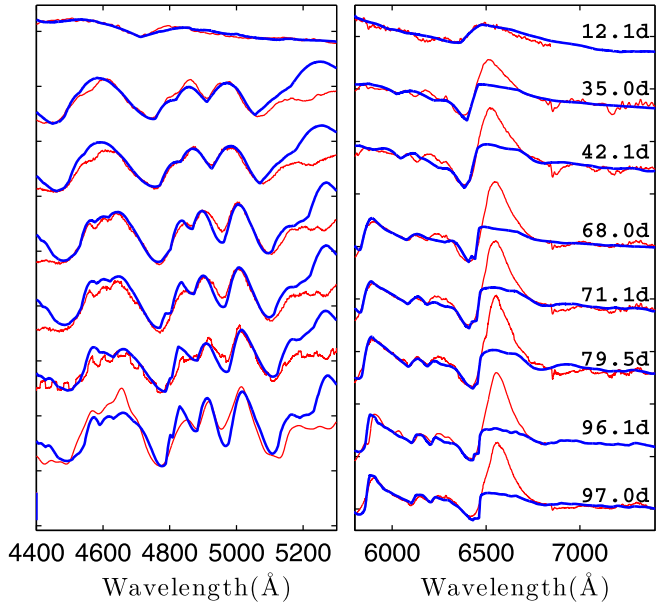

Figure 13. SYNOW modeling of SN 2013ej spectra at eight phases during 12–97 days for Hβ, Fe II multiplet (left), and Hα (right) profiles. Model spectra are shown with a thick solid line (blue), while the observed ones are shown with a thin solid line (red). In the model, H I lines are treated as detached to fit the absorption troughs. Along with Fe II and H I, other ions (Sc II, Ba II, Si ii, Na I, Ti II) are also incorporated into the model to fit some weaker features, especially at later phases. In addition to this, HV H I lines are also incorporated (42 days onward) to fit the extended Hα and Hβ absorption troughs. The 97-day spectra do not have an Hβ and Fe II wavelength region; hence, it is not shown here.

5.3. Evolution of Spectral Lines

Investigation of the spectral evolution sheds light on various important aspects of the SN, like interaction of ejecta with the circumstellar material, geometrical distribution of the expanding shell of ejecta, and formation of dust during late times. SN spectra are dominated by P Cygni profiles, which are direct indicators of expansion velocities, and they evolve with the velocity of the photosphere. As ejecta expand and opacity decreases, allowing photons to escape from deeper layers rich in heavier elements, we are able to see the emergence and growth of various spectral lines.

To illustrate the evolution of the Hα line, in Figure 14 a partial region of spectra is plotted in the velocity domain corresponding to rest wavelengths of Hα. At 12 days a broad P Cygni profile (FWHM ∼ 9500 km s^{-1}) is visible, which becomes narrower with time as the expansion slows down. The blueshifted absorption troughs are direct estimators of the expansion velocity of the associated line-forming layer. The emission peaks are found to be blueshifted (by ∼3200 km s^{-1} at 12 days), which progressively decreases with a decrease in expansion velocity, and almost settling to zero velocity when the SN starts to enter the nebular phase (97 days). Such blueshifted emission peaks, especially during early phases, are generic features observable in SN spectra, e.g., SN 1987 A (Hanuschik & Dachs 1987), SN 1998 A (Pastorello et al. 2005), SN 1999em (Elmhamdi et al. 2003), SN 2004et (Sahu et al. 2006), SN 2012aw (Bose et al. 2013), SN 2013ab (Bose et al. 2015). These features are tied to the density structure of the ejecta, which in turn controls the amount of occultation of the receding part of ejecta, resulting in biasing of the emission peak (Anderson et al. 2014a), which is not limited to Hα but applicable to all spectral lines. However, such a blueshift is clearly detected for Hα, whereas for most other lines emission profiles are weak and peaks are contaminated by adjacent P Cygni profiles. A detailed SN spectral synthesis code like CMFGEN (Dessart & Hillier 2005b) is capable of reproducing such blueshifted emission peaks.

As inferred from Figure 10, the spectral evolution of SN 2013ej is almost identical to other typical SNe IIP. However, the comparison of 35- and 68-day spectra indicates that Fe II lines are somewhat underdeveloped as compared to other SNe at similar phases. As seen in the 68-day comparison, the Fe II (λλ4924, 5018, 5169) absorption dips are significantly weaker in comparison to that seen in other SNe.

Another prominent and unusual feature is seen in nebular spectra at 109 and 125 days, on top of Hα emission, and the same is marked as feature A in Figure 14. This unusual dip results in an apparent blueshift of the emission peak, which is in fact larger than that seen in the last plateau spectra at 97 days. Such evolution is unexpected and against the general trend of emission peak evolution in SNe. The low resolution of these spectra prohibits us from investigating this feature in detail. This feature can be split into two emission components, one redshifted at 1200 km s^{-1} and another blueshifted by 1300 km s^{-1} (see the Appendix for further explanation) with respect to the Hα rest position. Such an asymmetric or double-peaked Hα nebular emission has been observed in a number of SNe,

Table 6
Line Velocities of Hα, Hβ, Fe II (λλ4924, 5018, 5169), and He I λ5876 as Estimated by Modeling the Observed Spectra of SN 2013ej with SYNOW. Fe II or He I Lines Velocities are Taken to Represent Photospheric Velocity (v_{phm})

UT Date (yyyy mm dd)	Phase[a] (day)	v(He I) (10^3 km s^{-1})	v(Fe II) (10^3 km s^{-1})	v(H$_\alpha$) (10^3 km s^{-1})	v(H$_\alpha$) HV[b] (10^3 km s^{-1})	v(H$_\beta$) (10^3 km s^{-1})	v(H$_\beta$) HV[b] (10^3 km s^{-1})
2013 Aug 04.86	12.1	8.8	...	9.6	...	9.7	...
2013 Aug 27.76	35.0	...	6.7	7.9	...	6.6	...
2013 Sep 03.90	42.1	...	5.8	7.2	8.5	5.4	6.4
2013 Sep 29.78	68.0	...	3.6	5.8	7.4	4.0	5.8
2013 Oct 02.89	71.1	...	3.3	5.4	7.3	3.8	5.8
2013 Oct 11.28	79.5	...	3.3	5.2	6.3	3.6	4.8
2013 Oct 27.87	96.1	...	2.7	4.9	6.3	3.5	4.8
2013 Oct 28.79	97.0	...	2.7	4.8	6.3	...	...

Notes.
[a] With reference to the time of explosion JD 2,456,497.30.
[b] High-velocity component used to fit the broad Hα and Hβ profile.

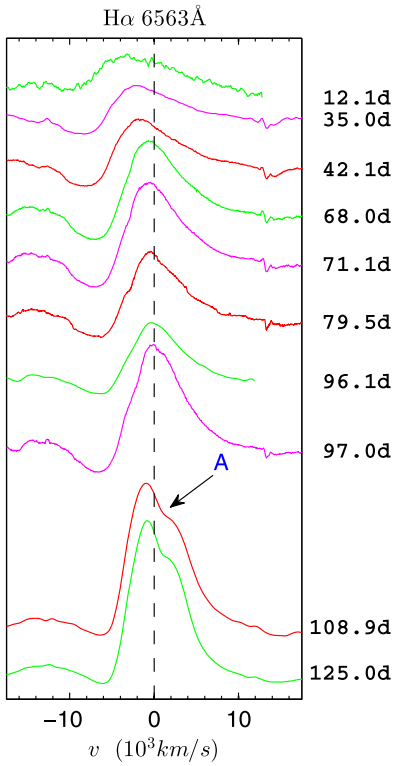

Figure 14. Evolution of Hα line profile at 10 phases during 12–125 days. A zero-velocity line is plotted with a dashed line corresponding to the rest wavelength of Hα λ6563.

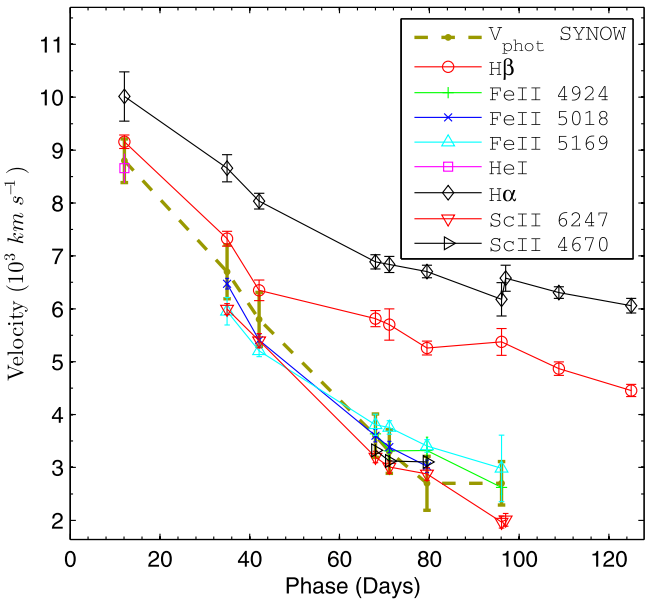

Figure 15. Velocity evolution of Hα, Hβ, He I, Sc II, and Fe II lines. The velocities are estimated using the blueshift of the absorption minima. The expansion velocities of the photosphere (v_{phm}) estimated from SYNOW modeling of He I line at 12 days and Fe II lines at later phases (see Table 6) are also overplotted for comparison.

e.g., SN 1999em (Leonard et al. 2002a) and SN 2004dj (Chugai et al. 2005). Leonard et al. (2002a) identified such a dip or notch in the Hα emission profile only during the nebular phase of SN 1999em, which they suggested as a possible ejecta–CSM interaction or asymmetry in the line-emitting region. In SN 2004dj, the asymmetry in nebular Hα spectra identified by Chugai et al. (2005) has been explained by bipolar distribution of ^{56}Ni with a spherical hydrogen envelope (Chugai 2006).

5.4. Ejecta Velocity

Progenitor stars prior to explosion develop stratified layers of different elements, which are generally arranged in an elemental sequence, hydrogen being abundant in the outermost shell, whereas heavier metals like iron predominate at deeper layers. However, at the time of shock breakout significant mixing of layers may occur. Spectral lines originating from different layers of the ejecta attain different characteristic velocities. Thus, study of velocity evolution provides important clues to the explosion geometry and the characteristics of various layers. Evolution of the photospheric layer is of special interest as it is directly connected to the kinematics and other related properties. The photosphere represents the layer of the SN atmosphere where optical depth attains a value of ∼2/3 (Dessart & Hillier 2005a). Due to complex mixing of layers and continuous recession of the recombination front, no single spectral line can represent the true photospheric layer. During the plateau phase, Fe II or Sc II lines are the best estimator of photospheric velocity (v_{ph}). In early phases, when

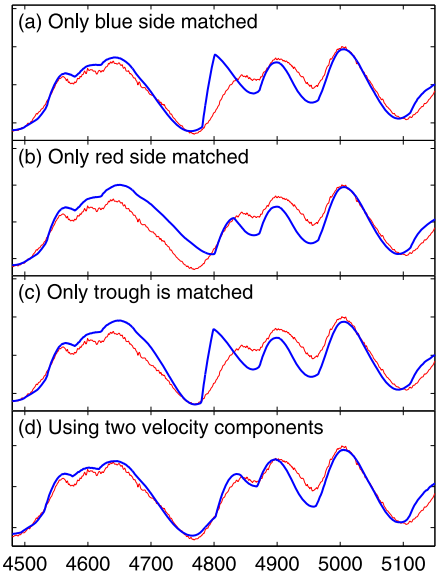

Figure 16. For the 68-day spectrum, the Hβ profile is fitted using SYNOW with various velocity components: (a) fit only with a single HV component to match the blue wing of the absorption dip, (b) with a single low-velocity component to match the red wing, (c) with a single velocity to only fit the trough, (d) with two velocity components to fit the entire absorption profile.

Fe II lines are not strongly detectable, the best proxy for $v_{\rm ph}$ is He I, or Hβ (Takáts & Vinkó 2012) in even earlier phases.

Line velocities can be estimated either by directly locating the P Cygni absorption troughs, as done using the SPLOT task of IRAF, or by modeling the line profiles with velocity as one of the inputs, as we do in SYNOW. In Figure 15, we plot the line velocities of Hα, Hβ, Fe II ($\lambda\lambda$4924, 5018, 5169), and Sc II ($\lambda\lambda$ 4670, 6247), using the absorption minima method. It is evident that Fe II and Sc II line velocities are very close to each other and are formed at deeper layers, whereas Hα and Hβ line velocities are consistently higher at all phases as they form at larger radii. The SYNOW estimated photospheric velocities are also plotted for comparison, which are very close to the Fe II and Sc II velocities estimated from the absorption minima method. Here the SYNOW-derived photospheric velocities are estimated by modeling the He I line for the 12-day spectrum and Fe II lines for the rest of the spectra. Velocities for various lines estimated using SYNOW are tabulated in Table 6.

Figure 17 shows the comparison of photospheric velocity of SN 2013ej with other well-studied SNe II, SN 1987 A, SN 1999em, SN 1999gi, SN 2004et, SN 2005cs, SN 2012aw, and SN 2013ab. For the purpose of comparison the absorption trough velocities have been used, taking the mean of the Fe II line triplet, or He I lines at early phases where Fe II lines are not detectable. The velocity profile of SN 2013ej is very similar to other normal SNe IIP, SN 1999em, SN 1999gi, SN 2004et, SN 2012aw, and SN 2013ab; on the other hand, velocities of SN 2005cs and SN 1987 A are significantly lower. The velocity profile of SN 2013ej is almost identical with SN 2004et, SN 2012aw, and SN 2013ab, whereas it is consistently higher than SN 1999gi and SN 1999em by ~800–900 km s^{-1}. For comparison of H I (Hα and Hβ) velocities, we have chosen all those events that are at least photometrically and spectroscopically similar to SN 2013ej. Comparison reveals that H velocities during later phases (60–100 days) are consistently higher than all comparable events. SN 2012aw and SN 2013ab have photospheric

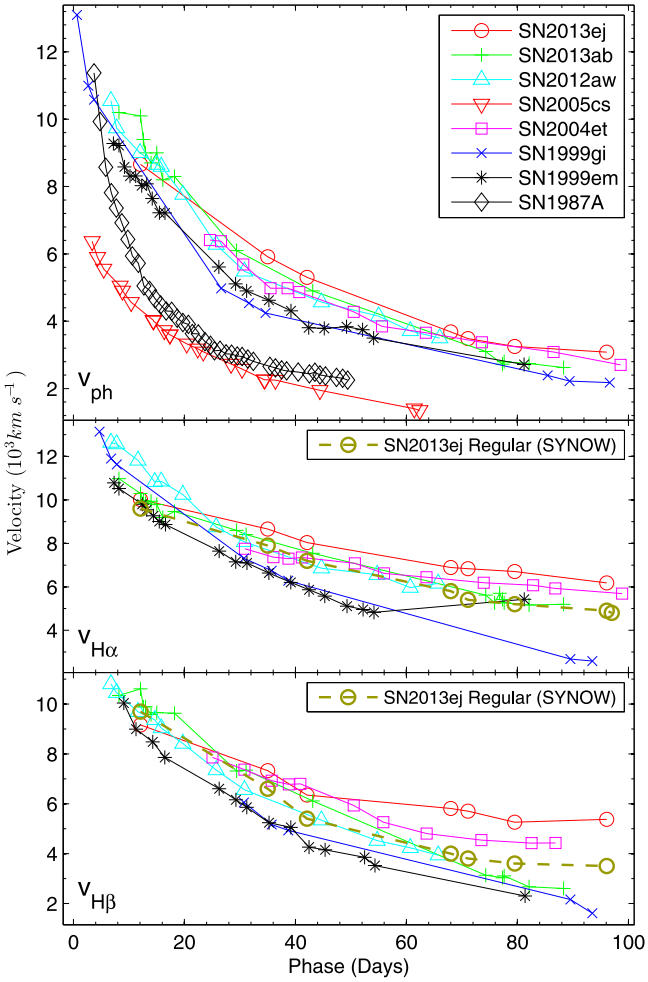

Figure 17. Photospheric velocity (top) evolution ($v_{\rm ph}$) of SN 2013ej compared with other well-studied SNe II. The $v_{\rm ph}$ plotted here are the absorption trough velocities (average of Fe II lines at late phases and He I at early phases). Similar comparisons of P Cygni absorption velocities, but for Hα and Hβ, are shown in the middle and bottom panels, respectively. The regular velocity components for Hα and Hβ estimated from SYNOW (without HV components; see Table 6) are also plotted for comparison.

velocities identical to SN 2013ej, but their H velocities are significantly lower by large values, e.g., for SN 2013ej the Hα velocity at 80 days is higher by 1500 km s^{-1} and Hβ is higher by 2400 km s^{-1}. Likewise, H velocities for SN 1999em and SN 1999gi are even lower at similar phases. Although SN 2004et H I velocities are somewhat on the higher end, they are still significantly less than those of SN 2013ej. It is also noted that, at 12 days, SN 2013ej H I velocities are consistent and similar to those of other normal SNe, but as it evolves, these velocities decline relatively slowly, ultimately turning into a higher velocity profile after ~40 days.

5.5. High-velocity Components of H I and CSM Interaction

As discussed in Section 5.2, the broad and extended Hα or Hβ absorption profiles are not properly reproduced using a single H I velocity component in SYNOW, and those profiles can only be fitted by incorporating HV components along with the regular one. Figure 16 shows the comparison of SYNOW fits for the 68-day Hβ profile with various single-velocity components, as well as for combined two-velocity components. A single-velocity component at 5600 km s^{-1} can match the blue wing

well and partially the trough, whereas it does not match the red side at all. Similarly, a single-velocity component at 4000 km s^{-1} can partially match the red slope of the trough, but it does not include the trough and the extended blue wing. By only matching the trough position, the model fits for a single velocity of 5300 km s^{-1}, which does not fit either the blue or the red wing. Even though the "detachment" of H I from the photosphere in the SYNOW model makes the fit of the red wing worse by steepening it further, it is still conclusive that none of these single-velocity components can properly reproduce the absorption profile. It is only by including two velocity components together in the model that we could reproduce the entire Hβ profile. Such a scenario starts to appear from the 42-day spectrum, which only becomes stronger as the line evolves until 97 days. The Hα troughs are also reproduced in a similar fashion. However, it may be noted that such an extended H I feature may also be explained as a possible outcome of a different (complex and extended) density profile that SYNOW cannot reproduce.

The comparison of Hα and Hβ velocities with other normal SNe IIP (see Figure 17), estimated by directly locating the P Cygni absorption troughs, shows that SN 2013ej velocities are significantly higher and decline relatively slowly (especially during later phases; 60–100 days) as compared to those seen in typical SNe IIP, e.g., SN 1999em, SN 1999gi, SN 2012aw, and SN 2013ab. On the other hand, the photospheric velocity comparison with other SNe IIP does not show any such anomaly. We suggest that this is the effect of blending with H I HV components in Hα and Hβ, which we could separate out while modeling these broad features with SYNOW having two velocity components. The regular Hα and Hβ velocities estimated from SYNOW decline at a normal rate consistent to that seen in other SNe (see Figure 17), whereas the HV components remain at higher velocities of 1000–2000 km s^{-1}, declining at a relatively slower rate. It is also interesting to note that the velocity difference between the regular and HV component for Hα and Hβ is similar at the same epochs. Chugai et al. (2007) identified similar HV absorption features associated closely with Hα and Hβ troughs in SN 1999em and SN 2004dj, which remained constant with time. The presence of such HV features has also been detected in SN 2009bw (Inserra et al. 2012) and SN 2012aw (Bose et al. 2013), which is suggestive of interaction of SN ejecta with preexistent CSM. Similar to SN 2013ej, HV signatures have been detected all throughout the plateau-phase evolution of SN 2009bw, while in SN 2012aw such features were only detected at the late plateau phase (55–104 days). Although we found HV components in SN 2013ej by modeling the extended P Cygni troughs, we are unable to visually detect two individual velocity components, which is possibly because of our signal-to-noise-ratio-limited spectra and weaker strength of HV components. Chugai et al. (2007) argued that SN ejecta can interact with the cooler dense shell of CMS material, which might have originated from the pre-SN mass loss in the form of stellar winds. Their analysis showed that such an interaction can lead to the detection of HV absorption features on bluer wings of Balmer lines due to enhanced excitation of the outer layers of unshocked ejecta. We therefore suggest a weak or moderate ejecta–CSM interaction in SN 2013ej. X-ray emission from SN 2013ej has also been reported by Margutti et al. (2013), who measured a 0.3–10 keV count rate of 2.7 ± 0.5 cps, translating into a flux of $\sim 1.1 \times 10^{-13}$ erg s^{-1}cm^{-2} (assuming a simple power-law spectral model with photon index Gamma = 2). Such X-ray emission may also indicate an ejecta–CSM interaction suffered by SN 2013ej.

6. STATUS OF SN 2013ej IN TYPE II DIVERSITY

6.1. Factors Favoring SN 2013ej as Type IIL

Having characterized the event both photometrically and spectroscopically, we may now revisit the aspects that favor SN 2013ej as a Type IIL event. The SN was originally classified as Type IIP (Valenti et al. 2013) based on spectroscopic similarity to SN 1999gi. Due to the same underlying physical mechanisms that govern both Type IIP and IIL SNe, early spectra may not clearly distinguish these subclasses of SNe II. The distinguishing factor among IIP and IIL is nominal and mainly depends on light-curve characteristics. SN 2013ej shows a decline of 1.74 mag (100 days)$^{-1}$ (see Table 5) or ~0.87 mag in 50 days, which definitely falls in the criteria of SNe IIL as proposed by Faran et al. (2014). In Figure 4, the spread of template light curves for Type IIP and IIL (Faran et al. 2014) is shown along with M_V light curves of the SN sample. It is evident that under this scheme of classification, SN 2013ej is not a Type IIP; rather, it is marginally within the range of Type IIL template light curves. This is also justified from the point of the basic idea behind these classifications, that Type IIP must show a "plateau" of almost constant brightness for some time (~90 days), which is not the case with SN 2013ej. Due to the very fact that SN II light curves and physical properties exhibit a continuum distribution rather than a bi-modality (Anderson et al. 2014b), SN 2013ej shows intermediate characteristics in the SN II diversity.

One distinguishing spectroscopic property Faran et al. (2014) found for SNe IIL is the overall higher photospheric (Fe II λ5196) velocity and flatter H I (Hβ and Hα) velocity profiles as compared to Type IIP counterparts. Although Fe II velocities are on the higher end as compared to typical SN IIP velocities, we do not find it to be a remarkable enough deviation to distinguish SN 2013ej from the Type IIP sample. However, we do see an anomaly in Hα and Hβ absorption minima velocity profiles, as they start off with velocities consistent with those of Type IIP but decline relative slowly (see Section 5.4 for more details of this feature), ultimately surpassing faster-declining IIP velocity profiles after 50 days. This characteristic feature of H I velocities for SN 2013ej is typical for most SNe IIL, as found by Faran et al. (2014).

6.2. CSM Interaction and Type IIL

Faran et al. (2014) proposed a possible explanation for the flatter velocity profiles in SNe IIL, which is due to the lack of hydrogen in deeper and slow-expanding layers of ejecta, resulting in higher H I absorption velocities arising mostly from the outer layer. However, for SN 2013ej we suggest that the flattening of Hα and Hβ velocity profiles is due to the contamination of the HV component of H I (see Section 5.5). An indication of CSM interaction in SN 2013ej may also be inferred from X-ray detection by Margutti et al. (2013). Valenti et al. (2015) found SN 2013by, a Type IIL SN, to be moderately interacting with CSM. This led them to question the prevalence of the CSM interaction among SNe IIL in general. SNe IIL originate from progenitors similar to IIPs but have lost a significant fraction of hydrogen before explosion during pre-SN evolution. Hence, it may not be usual to detect

HV H I signatures in Hα and Hβ absorption profiles as a consequence of ejecta–CSM interaction. A moderate or weak interaction may produce an HV component blending with Hα and Hβ profiles, which may result in a shift in absorption minima, rather than a prominent secondary HV dip. Such a scenario may perfectly explain the relatively higher and flatter H I velocity profiles of most SNe IIL as compared to IIP counterparts, found by Faran et al. (2014) based on direct velocity estimates of absorption minima.

Another example of CSM interaction in Type IIL is SN 2008fq, which does show a strong interaction signature like a Type IIn (Taddia et al. 2013), but also shows a steep decline like IIL during the first 60 days (Faran et al. 2014). PTF11iqb (Smith et al. 2015) is also an SN IIn, having prominent CSM interaction signatures, but with signatures of IIL like a steeper light curve. Initial spectra of this SN showed IIn characteristics; however, late plateau spectra revealed features similar to Type IIL. PTF11iqb originated from a progenitor identical to Type IIP/L, instead of a luminous blue variable as expected for a typical IIn. However, because of the rare detection of Type IIL events and the fast decline in magnitudes, we do not have sufficient information to investigate a CSM interaction in all such objects. Thus, the question still remains open whether all or most SNe IIL interact with CSM and whether the flatter H I absorption minima velocity profiles are a consequence of interaction.

7. LIGHT-CURVE MODELING

To determine the explosion parameters of SN 2013ej, the observed light curve is modeled following the semianalytical approach originally developed by Arnett (1980) and further refined in Arnett & Fu (1989). A more appropriate and accurate approach would have been detailed hydrodynamical modeling (e.g., Falk & Arnett 1977; Utrobin 2007; Bersten et al. 2011; Pumo & Zampieri 2011) to determine explosion properties; however, application of simple semianalytical models (Arnett 1980, 1982; Arnett & Fu 1989; Popov 1993; Zampieri et al. 2003; Chatzopoulos et al. 2012) can be useful to get preliminary yet reliable estimates of the parameters without running resource-intensive and time-consuming hydrodynamical codes. Nagy et al. (2014) also followed the original semianalytical formulation presented by Arnett & Fu (1989) and modeled a few well-studied SNe II. The results are compared with hydrodynamical models from the literature and are found to be in good agreement. The model light curve is computed by solving the energy balance of the spherically symmetric SN envelope, which is assumed to be in homologous expansion, having a spatially uniform density profile.

The temperature evolution is given as (Arnett 1980)

$$T(x,\,t)^4 = T_0^4\,\psi(x)\,\phi(t)\left(\frac{R_0}{R(t)}\right)^4,$$

where x is defined as the dimensionless co-moving radius relative to the mass of the envelope and $\psi(x)$ is the radial component of the temperature profile, which falls off with radius as $\sin(\pi x)/\pi x$. Here we incorporate the effect of recombination, as the shock-heated and ionized envelope expands and cools down to recombine at temperature $T_{\rm rec}$. We define x_i as the co-moving radius of the recombination front, and the opacity (κ) changes very sharply at this layer such that $\kappa \approx 0$ for the ejecta above x_i. Following the treatment

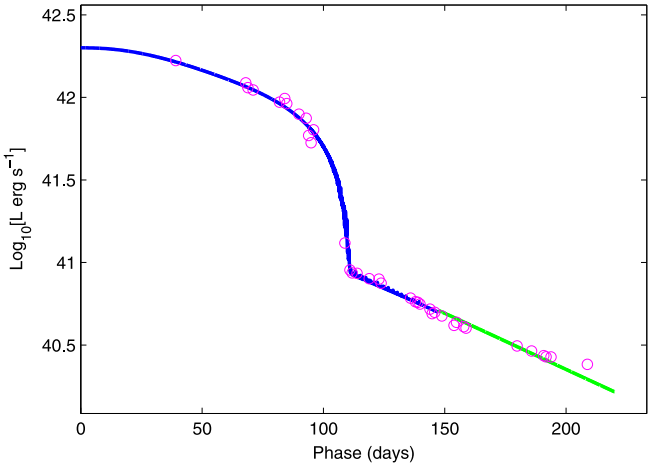

Figure 18. Model fit (solid line) on the observed bolometric light curve (open circles) of SN 2013ej. The green solid line follows only the radioactive decay law, where the recombination front has completely disappeared.

of Arnett & Fu (1989), the temporal component of temperature $\phi(t)$ can be expressed as (Nagy et al. 2014)

$$\frac{d\phi(t)}{dz} = \frac{R(t)}{R_0 x_i^3}\left[p_1\zeta(t) - p_2\,\phi(t)x_i - 2x_i^2\,\phi(t)\frac{R_0}{R(t)}\frac{dx_i}{dz}\right],$$

where $\zeta(t)$ is the total radioactive energy input from the decay chain of unit mass of ^{56}Ni, which is normalized to the energy production rate of ^{56}Ni. The rest of the parameters in the equation have the usual meaning and can be found in aforementioned papers. From this ordinary differential equation we can find out the solution of $\phi(t)$ using the Runge–Kutta method. The treatment adopted to determine x_i is somewhat similar to that in Nagy et al. (2014), where we numerically determine the radius x_i (to an accuracy of 10^{-12}) for which the temperature of the layer reaches $T_{\rm rec}$. Once we find out the solution of $\phi(t)$ and x_i, the total bolometric luminosity is calculated as the sum of radioactive heating and the rate of energy released due to recombination,

$$L(t) = x_i\frac{\phi(t)E_{\rm th}(0)}{\tau_d}\left(1 - e^{-A_g/t^2}\right) + 4\pi r_i^2 Q\rho(x_i,\,t)R(t)\frac{dx_i}{dt},$$

where $d(x_i)/dt$ is the inward velocity of the co-moving recombination front and the term $[1 - \exp(-A_g/t^2)]$ takes into account gamma-ray leakage from the ejecta. The factor A_g is the effectiveness of gamma-ray trapping (see e.g., Clocchiatti & Wheeler 1997; Chatzopoulos et al. 2012), where large A_g means full trapping of gamma rays; this factor is particularly important to model the SN 2013ej tail light curve. In this relation we also modified the second term to correctly account for the amount of envelope mass being recombined.

To model SN light curves, it is essential to obtain the true bolometric luminosity from observations. Since our data are limited only to optical and UV bands, we adopt the prescription for color-dependent bolometric corrections by Bersten & Hamuy (2009) to obtain the bolometric light curve for SN 2013ej. Figure 18 shows the model fit with the observed bolometric light curve of the SN. We estimate an ejecta mass of 12 $M_\odot$, progenitor radius of 450 $R_\odot$, and explosion energy (kinetic + thermal) of 2.3 foe (10^{51} erg). The uncertainty in

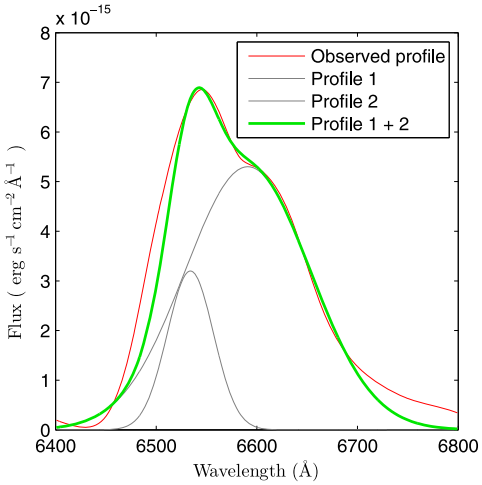

Figure 19. Hα profile of 125-day spectrum fitted by two component Gausian profiles seperated by ∼2500 km s^{-1}.

mass and radius is about 25%. We find that the plateau duration is strongly correlated with explosion energies (especially kinetic) and also with κ and $T_{\rm rec}$. Thus, depending on these parameters, our model is consistent with a wide range of explosion energies, with 2.3 foe toward the lower end and energies up to 4.5 foe at higher end. Assuming the mass of the compact remnant to be 1.5–2.0 $M_{\odot}$, the total progenitor mass adds up to be 14 $M_{\odot}$.

The mass of radioactive ^{56}Ni estimated from the model is 0.018 $M_{\odot}$, which primarily governs the tail light curve of the SN. As discussed in Section 4.2, the slope of the tail light curve observed for SN 2013ej is significantly higher than other typical SNe IIP and also that expected from radioactive decay of ^{56}Co to ^{56}Fe. The light curve powered by full gamma-ray trapping from the radioactive decay chain of ^{56}Ni → ^{56}Co → ^{56}Fe results in a slower decline and does not explain the steeper tail observed in SN 2013ej. In the model we decreased the gamma-ray trapping effectiveness parameter A_g to 3×10^4 days^2, which matches the steeper radioactive tail. The gamma-ray optical depth can be related to this parameter as $\tau_g \sim A_g / t^2$. This implies that the gamma-ray leakage in SN 2013ej is significantly higher than in other typical SNe IIP.

Valenti et al. (2014), using early temperatures (<5 days) of SN 2013ej, provided a preliminary estimate of the progenitor radius as 400–600 $R_{\odot}$, which is in good agreement with our result. Our progenitor mass estimate is also consistent with that reported by Fraser et al. (2014) from direct observational identification of the progenitor using *HST* archival images, which is 8–15.5 $M_{\odot}$.

8. SUMMARY

We present photometric and spectroscopic observations of SN 2013ej. Despite low-cadence optical photometric follow-up during photospheric phase, we are able to cover most of the important phases and features of the light curve.

Our high-resolution spectrum at 80 days shows the presence of the Na I D (λλ5890, 5896) doublet for the Milky Way, but no impression for host galaxy NGC 0628. This indicates that SN 2013ej suffers minimal or no reddening due to its host galaxy.

The optical light curves are similar to SNe IIL, with a relatively short plateau duration of 85 days and steeper decline rates of 6.60, 3.57, 1.74, 1.07, and 0.74 mag (100 days^{-1}) in *UBVRI* bands, respectively. The comparison of absolute *V*-band light curves shows that SN 2013ej suffers a higher decline rate than all SNe IIP, but similar to SNe IIL SN 1980 k, SN 2000dc, and SN 2013by. The drop in luminosity during the plateau-nebular transition is also higher than most SNe II in our sample, which is 2.4 mag in *V* band.

The UVOT UV–optical light curves show a steep decline during the first 30 days at a rate of 0.182, 0.213, and 0.262 mag day^{-1} in *uvw*1, *uvw*2, and *uvm*2 bands, respectively. The absolute UV light curves are identical to SN 2012aw and also show a similar UV-plateau trend as observed in SN 2012aw.

Owing to the large drop in luminosity during the plateau-nebular transition, the light curve settles to a significantly low luminosity tail phase as compared to other normal SNe IIP. The mass of radioactive ^{56}Ni estimated from the tail bolometric luminosity is 0.020 ± 0.002 $M_{\odot}$, which is in between normal SNe IIP (e.g., SN 1999em, SN 2004et, SN 2012aw) and subluminous events, like SN 2005cs.

The spectroscopic features and their evolution are similar to normal Type II events. Detailed SYNOW modeling has been performed to identify spectral features and to estimate velocities for Hα, Hβ, Fe II (λλ4924, 5018, 5169), and Sc II (λλ4670, 6247) lines. The photospheric velocity profile of SN 2013ej, which is represented by Fe II lines and He I lines at 12 days, is almost identical to that of SN 2004et, SN 2012aw, and SN 2013ab. The Hα and Hβ velocities estimated by directly locating the absorption troughs are significantly higher and slow declining as compared to other normal IIP events. However, such H I velocity profiles are typical for SNe IIL.

The P Cygni absorption troughs of Hα and Hβ are found to be broad and extended, which a single H I component in SYNOW model could not fit properly. However, these extended features are fitted well with SYNOW by incorporating an HV H I component. These HV components can be traced throughout the photospheric phase, which may indicate a possible ejecta–CSM interaction. Our inference is also supported by the detection of X-ray emission from SN 2013ej (Margutti et al. 2013), indicating a possible CSM interaction, and the unusually high polarization reported by Leonard et al. (2013) may also further indicate asymmetry in the environment or ejecta of the SN. Such a CSM interaction and their signature in Hα and Hβ profiles have also been reported for SN 2009bw (Inserra et al. 2012) and SN 2012aw (Bose et al. 2013).

Nebular-phase spectra during 109–125 days are dominated by characteristic emission lines; however, the Hα line shows an unusual notch, which may be explained by superposition of HV emission on a regular Hα profile. Although the origin of the feature is not fully explained, it may indicate bipolar distribution of ^{56}Ni in the core.

We modeled the bolometric light curve of SN 2013ej and estimated a progenitor mass of ∼14 $M_{\odot}$, radius of ∼450 $R_{\odot}$, and explosion energy of ∼2.3 foe. These progenitor property estimates are consistent with those given by Fraser et al. (2014) and Valenti et al. (2014) for mass and radius, respectively. The tail bolometric light curve of SN 2013ej is found to be significantly steeper than that expected from the decay chain of radioactive ^{56}Ni. Thus, in the model we decreased the effectiveness of gamma-ray trapping, which could explain the steeper slope of the tail light curve.

We are thankful to the observing staffs and technical assistants of the ARIES 1.0 and 1.3 m telescopes, and we also express our thanks to 2 m HCT telescope staffs for their kind cooperation in observation of SN 2013ej. We also express our thanks to Mr. Shashank Shekhar for his sincere efforts and cooperation during observations at the ARIES 1.3 m telescope. Authors gratefully acknowledge the services of the NASA ADS and NED databases, which are used to access data and references in this paper. SOUSA is supported by NASA's Astrophysics Data Analysis Program through grant NNX13AF35G. V.V.D.'s work on Type IIP SNe is supported by NASA through Chandra Award No. GO2-13092B issued by *Chandra X-Ray Observatory Center*, which is operated by the Smithsonian Astrophysical Observatory for and on behalf of NASA under contract NAS8-03060. We also thank the anonymous referee for detailed and insightful comments that helped significantly improve the manuscript.

APPENDIX
NEBULAR Hα PROFILE

The unusual notch in the nebular Hα profile can be described as a superimposition of two profiles. Figure 19 shows the observed Hα profile at 125 days, which is fitted by two component Gaussian profiles. These two profiles are separated by 55 Å (~2500 km s^{-1}), one being blueshifted by −1300 km s^{-1} while the other is redshifted at 1200 km s^{-1} with respect to the rest Hα position. The FWHM for the blue component is 54Å and for the red component is 146 Å. The redshifted component is dominant in strength over the blue one, having a ratio of EWs of 4.5. It may be noted that, for the sake of simplicity and only for the purpose of illustration, we used Gaussian profiles, which does not account for the P Cygni absorption troughs we see on bluer wings of line profiles in observed SN spectra.

REFERENCES

Anderson, J. P., Dessart, L., Gutierrez, C. P., et al. 2014a, MNRAS, 441, 671
Anderson, J. P., González-Gaitán, S., Hamuy, M., et al. 2014b, ApJ, 786, 67
Arcavi, I., Gal-Yam, A., Cenko, S. B., et al. 2012, ApJL, 756, L30
Arnett, D. 1996, Supernovae and Nucleosynthesis: An Investigation of the History of Matter from the Big Bang to the Present (Princeton, NJ: Princeton Univ. Press)
Arnett, W. D. 1980, ApJ, 237, 541
Arnett, W. D. 1982, ApJ, 253, 785
Arnett, W. D., & Fu, A. 1989, ApJ, 340, 396
Barbon, R., Benetti, S., Rosino, L., Cappellaro, E., & Turatto, M. 1990, A&A, 237, 79
Barbon, R., Ciatti, F., & Rosino, L. 1979, A&A, 72, 287
Barbon, R., Ciatti, F., & Rosino, L. 1982, A&A, 116, 35
Bayless, A. J., Pritchard, T. A., Roming, P. W. A., et al. 2013, ApJL, 764, L13
Bersten, M. C., Benvenuto, O., & Hamuy, M. 2011, ApJ, 729, 61
Bersten, M. C., & Hamuy, M. 2009, ApJ, 701, 200
Blinnikov, S. I., & Bartunov, O. S. 1993, A&A, 273, 106
Bose, S., & Kumar, B. 2014, ApJ, 782, 98
Bose, S., Kumar, B., Sutaria, F., et al. 2013, MNRAS, 433, 1871
Bose, S., Valenti, S., Misra, K., et al. 2015, MNRAS, 450, 2373
Branch, D., Benetti, S., Kascn, D., et al. 2002, ApJ, 566, 1005
Breeveld, A. A., Landsman, W., Holland, S. T., et al. 2011, in AIP Conf. Ser. 1358, ed. J. E. McEnery, J. L. Racusin, & N. Gehrels (Melville, NY: AIP), 373
Brown, P. J., Breeveld, A. A., Holland, S., Kuin, P., & Pritchard, T. 2014, Ap&SS, 354, 89
Brown, P. J., Holland, S. T., lmmler, S., et al. 2009, AJ, 137, 4517
Burrows, A. 2013, RvMP, 85, 245
Chatzopoulos, E., Wheeler, J. C., & Vinko, J. 2012, ApJ, 746, 121
Chugai, N. N. 2006, AstL, 32, 739
Chugai, N. N., Chevalier, R. A., & Utrobin, V. P. 2007, ApJ, 662, 1136
Chugai, N. N., Fabrika, S. N., Sholukhova, O. N., et al. 2005, AstL, 31, 792
Clocchiatti, A., & Wheeler, J. C. 1997, ApJ, 491, 375
Dessart, L., Blondin, S., Brown, P. J., et al. 2008, ApJ, 675, 644
Dessart, L., & Hillier, D. J. 2005a, A&A, 437, 667
Dessart, L., & Hillier, D. J. 2005b, in ASP Conf. Ser. 332, The Fate of the Most Massive Stars, ed. R. Humphreys & K. Stanek (San Francisco, CA: ASP), 415
Dwarkadas, V. V. 2014, MNRAS, 440, 1917
Elmhamdi, A., Danziger, I. J., Chugai, N., et al. 2003, MNRAS, 338, 939
Falk, S. W., & Arnett, W. D. 1977, ApJS, 33, 515
Faran, T., Poznanski, D., Filippenko, A. V., et al. 2014, MNRAS, 445, 554
Fisher, A., Branch, D., Hatano, K., & Baron, E. 1999, MNRAS, 304, 67
Fisher, A., Branch, D., Nugent, P., & Baron, E. 1997, ApJL, 481, L89
Fraser, M., Maund, J. R., Smartt, S. J., et al. 2014, MNRAS, 439, L56
Gehrels, N., Chincarini, G., Giommi, P., et al. 2004, ApJ, 611, 1005
Gutiérrez, C. P., Anderson, J. P., llamuy, M., et al. 2014, ApJL, 786, L15
Hamuy, M. 2003, ApJ, 582, 905
Hamuy, M., & Suntzeff, N. B. 1990, AJ, 99, 1146
Hanuschik, R. W., & Dachs, J. 1987, A&A, 182, L29
Heger, A., Fryer, C. L., Woosley, S. E., Langer, N., & Hartmann, D. H. 2003, ApJ, 591, 288
Hendry, M. A., Smartt, S. J., Maund, J. R., et al. 2005, MNRAS, 359, 906
Herrmann, K. A., Ciardullo, R., Feldmeier, J. J., & Vinciguerra, M. 2008, ApJ, 683, 630
Inserra, C., Baron, E., & Turatto, M. 2012a, MNRAS, 422, 1178
Inserra, C., Turatto, M., Pastorello, A., et al. 2011, MNRAS, 417, 261
Inserra, C., Turatto, M., Pastorello, A., et al. 2012b, MNRAS, 422, 1122
Kim, M., Zheng, W., Li, W., et al. 2013, CBET, 3606, 1
Krisciunas, K., Hamuy, M., Suntzeff, N. B., et al. 2009, AJ, 137, 34
Lee, M., Li, K. L., Wang, J.-W., et al. 2013, ATel, 5466, 1
Leonard, D. C., Filippenko, A. V., Gates, E. L., et al. 2002a, PASP, 114, 35
Leonard, D. C., Filippenko, A. V., Li, W., et al. 2002b, AJ, 124, 2490
Leonard, D. C., Kanbur, S. M., Ngeow, C. C., & Tanvir, N. R. 2002c, BAAS, 34, 1143
Leonard, P. B. D. C., Pignata, G., Dessart, L., et al. 2013, ATel, 5275, 1
Litvinova, I. Y., & Nadezhin, D. K. 1985, SvAL, 11, 145
Maguire, K., DiCarlo, E., Smartt, S. J., et al. 2010, MNRAS, 404, 981
Margutti, R., Chakraborti, S., Brown, P. J., & Sokolovsky, K. 2013, ATel, 5243, 1
Marion, G. H., Vinko, J., Kirshner, R. P., et al. 2014, ApJ, 781, 69
Milisavljevic, D., Margutti, R., Soderberg, A. M., et al. 2013, ApJ, 767, 71
Nagy, A. P., Ordasi, A., Vinkó, J., & Wheeler, J. C. 2014, A&A, 571, A77
Olivares, E. F., Hamuy, M., Pignata, G., et al. 2010, ApJ, 715, 833
Pastorello, A., Baron, E., Branch, D., et al. 2005, MNRAS, 360, 950
Pastorello, A., Valenti, S., Zampieri, L., et al. 2009, MNRAS, 394, 2266
Popov, D. V. 1993, ApJ, 414, 712
Poznanski, D., Ganeshalingam, M., Silverman, J. M., & Filippenko, A. V. 2011, MNRAS, 415, L81
Poznanski, D., Prochaska, J. X., & Bloom, J. S. 2012, MNRAS, 426, 1465
Pumo, M. L., & Zampieri, L. 2011, ApJ, 741, 41
Richmond, M. W. 2014, JAVSO, 42, 333
Roming, P. W. A., Kennedy, T. E., Mason, K. O., et al. 2005, SSRv, 120, 95
Sahu, D. K., Anupama, G. C., Srividya, S., & Muneer, S. 2006, MNRAS, 372, 1315
Sanders, N. E., Soderberg, A. M., Gezari, S., et al. 2015, ApJ, 799, 208
Schlafly, E. F., & Finkbeiner, D. P. 2011, ApJ, 737, 103
Shappee, B. J., Kochanek, C. S., Stanek, K. Z., et al. 2013, ATel, 5237, 1
Smartt, S. J. 2009, ARA&A, 47, 63
Smith, N., Mauerhan, J. C., Cenko, S. B., et al. 2015, MNRAS, 449, 1876
Spiro, S., Pastorello, A., Pumo, M. L., et al. 2014, MNRAS, 439, 2873
Taddia, F., Stritzinger, M. D., Sollerman, J., et al. 2013, A&A, 555, A10
Takáts, K., Pumo, M. L., Elias-Rosa, N., et al. 2014, MNRAS, 438, 368
Takáts, K., & Vinkó, J. 2012, MNRAS, 419, 2783
Tomasella, L., Cappellaro, E., Fraser, M., et al. 2013, MNRAS, 434, 1636
Turatto, M., Benetti, S., & Cappellaro, E. 2003, in From Twilight to Highlight: The Physics of Supernovae, ed. W. Hillebrandt & B. Leibundgut (Berlin: Springer), 200
Utrobin, V. P. 2007, A&A, 461, 233
Valenti, S., Sand, D., Howell, D. A., et al. 2013, ATel, 5228, 1
Valenti, S., Sand, D., Pastorello, A., et al. 2014, MNRAS, 438, L101
Valenti, S., Sand, D., Stritzinger, M., et al. 2015, MNRAS, 448, 2608
van Dokkum, P. G. 2001, PASP, 113, 1420
Wang, S. I., Hildebrand, R. H., Hobbs, L. M., et al. 2003, Proc. SPIE, 4841, 1145
Zampieri, L., Pastorello, A., Turatto, M., et al. 2003, MNRAS, 338, 711